Melt inclusions at MT. Edixon (Antarctica): Chemistry, petrology and implications for the evolution of the Lanterman range

Fabio Ferri [a], Bernardo Cesare [a,*], Omar Bartoli [a], Silvio Ferrero [b,c], Rosaria Palmeri [d], Laurent Remusat [e], Stefano Poli [f]

[a] Department of Geosciences, University of Padua, Italy
[b] Institute of Geosciences, University of Potsdam, Germany
[c] Museum für Naturkunde (MfN), Leibniz-Institut für Evolutions und Biodiversitätsforschung, 10115 Berlin, Germany
[d] Museo Nazionale dell'Antartide, Sezione Scienze della Terra, Siena, Italy
[e] Muséum National d'Histoire Naturelle, Sorbonne Université, CNRS UMR 7590, Institut de Minéralogie, Physique des Matériaux et Cosmochimie, Paris, France
[f] Department of Earth Sciences, University of Milan, Italy

ARTICLE INFO

Article history:
Received 6 January 2020
Received in revised form 5 July 2020
Accepted 9 July 2020
Available online 18 July 2020

Keywords:
Melt inclusions
Crustal anatexis
Nanogranitoids
Antarctica
Lanterman range

ABSTRACT

The recovery of melt inclusions (MI) in peritectic phases of metamorphic rocks demonstrates their anatectic origin even in the absence of other textural or field evidences, and gives the opportunity to retrieve the chemical composition of primary melts and infer melt entrapment conditions. Here we report the first recovery of such inclusions in a medium-grade schist from the Edixon Metamorphic Complex (EMC) of the Lanterman Range in northern Victoria Land, Antarctica. This is the first study of melt inclusions from an Al_2SiO_5-free, graywacke-type protolith. Inclusions are hosted in garnet. They are both polycrystalline nanogranitoids, i.e., crystallized former MI, and fluid inclusions (FI) coexisting in the same clusters and displaying frequent negative crystal shape and textures indicative of a primary origin. The MI contain albite, K-feldspar, quartz, muscovite, biotite ± calcite ± siderite ± H_2O, while the FI are composed by $CO_2 + H_2O + N_2 + CH_4 \pm H_2S$ and contain step-daughter calcite. The schist hosting the garnets with melt inclusions contains muscovite, biotite, garnet, plagioclase, K-feldspar, and quartz. Extensive resorption of garnet and replacement by biotite, along with composition of micas that suggest medium-temperature, subsolidus conditions, indicate that after anatexis the schist was thoroughly recrystallized under retrograde conditions. The MI were remelted in a piston cylinder apparatus at conditions of 740–900 °C at 0.8–1.0 GPa with complete remelting taking place at 760–780 °C. The remelted glass is subalkaline, peraluminous (ASI ≈ 1.3–1.5) with CaO ≈ 1.2–2.1 wt% and K_2O ≈ 3.4–4.1 wt% and contains ≈ 4.3–5.3 wt% of H_2O and 400–1150 ppm of CO_2. The P-T conditions of melt entrapment were retrieved combining results of experimental remelting with calculated phase equilibria in the MnCNKFMASHT model system, and are between 740 and 780 °C and 0.7 to 0.9 GPa. The new and different P-T conditions for a high grade rock of the EMC with respect to other published data, confirm that this metamorphic complex is not homogeneous, and that anatexis may have taken place at different crustal levels during the evolution of the Cambro-Ordovician Ross Orogen.

1. Introduction

The discovery of primary melt inclusions (MI) hosted in peritectic minerals from high grade metamorphic rocks has been described in recent papers (reviewed by Cesare et al., 2015; Bartoli et al., 2016a; Bartoli and Cesare, 2020) and new examples are continuously adding from typical felsic crustal compositions or mafic to ultramafic ones (Ferrero et al., 2018). The MI represent a window into the anatectic history of partially melted terranes (Acosta-Vigil et al., 2010), and may provide key microstructural and compositional information on crustal anatexis, like mechanisms and nature of the melting process, pressure (P) – temperature (T) conditions of entrapment and melting, timeframes of melt production and segregation (Cesare et al., 2015). In the absence of other microstructural evidence of anatexis such as pseudomorphs after melt films or euhedral crystals bounded by growth facets (Holness et al., 2011), the MI become a unique tool to infer past melting events throughout the metamorphic history of a rock (Cesare et al., 2015). When MI coexist with fluid inclusions (FI), they are able to shed light on the fluid/melt/rock interactions during anatexis, and recent works demonstrated that melting processes are more commonly fluid-present than traditionally expected (Carvalho et al., 2019, 2020). The

combination of MI and FI studies can also help understanding the exchange, transport and recycling of volatile species (especially CO_2) in crustal evolution or during subduction.

In Antarctica, the presence of felsic-nanogranite inclusions produced after cooling of MI has been documented in garnets from the Lutzow-Holm Complex (East Antarctica, Hiroi et al., 2019) and Dronning Maud Land (East Antarctica, Ferrero et al., 2018), but not in the crystalline rocks of the northern Victoria Land, which have been studied mostly for their high-P evolution and where research on high-T processes has not been made in the last twenty years. Here we report the recovery of MI preserved in metapelitic garnets from the Edixon Metamorphic Complex (Lanterman Range, Fig. 1). This is the first discovery and study of nanogranitoids from rocks of the northern Victoria Land. In this research MI turn out to be the only tool allowing identification of anatexis in garnet-biotite-muscovite schists that would otherwise be interpreted as having undergone an entirely subsolidus evolution. This is also the first study of nanogranitoids formed by anatexis of an Al_2SiO_5-free metasedimentary protolith, providing further constraints on the composition of natural melts produced by anatexis of Al-poor pelitic rocks. The study of MI in garnet, together with the petrological study of their host rocks, also provides new clues to the geodynamic evolution of this crystalline basement.

2. Sample description

2.1. Geological setting

The Ross-Delamerian orogenic belt is one of the Earth's great Phanerozoic mountain belts resulting from convergence along the paleo-Pacific margin of Gondwana (Boger, 2011; Cawood, 2005). In Antarctica, the northern Victoria Land (Fig. 1A, B) represents one of the major segments of the Ross orogenic belt (e.g., Goodge, 2020; Stump, 1995).

From east to west, the northern Victoria Land is divided into three contrasting lithotectonic units with NW-SE structural trends (Bradshaw and Laird, 1983): 1) the Robertson Bay Terrane, 2) the Bowers Terrane and 3) the Wilson Terrane (Fig. 1B). The internal Wilson Terrane consists of low-P/high-T metamorphic rocks (Palmeri et al., 1991) with local remnants of a polymetamorphic granulite complex (Talarico et al., 1995). Metamorphic rocks are intruded by the *syn*-to post tectonic granitoids of the Granite Harbour Intrusive Complex considered to be a Cambro-Ordovician orogenic association with Ediacaran precursors (Bomparola et al., 2006; Borg et al., 1990; Ghezzo et al., 1989; Goodge, 2020; Kleinschmidt and Tessensohn, 1987).

Intermediate- to (ultra-)high-P metamorphic rocks including eclogites are present in the eastern Wilson Terrane along the Lanterman fault (Di Vincenzo et al., 1997; Di Vincenzo et al., 2016; Ghiribelli et al., 2002; Grew et al., 1984; Ricci and Tessensohn, 2003).

The Lanterman fault separates the Wilson Terrane from the Bowers Terrane and is best exposed at the Lanterman Range to the north and the Mountaineer Range to the south (Fig. 1B). From west to east, three different lithotectonic units have been identified in the Lanterman (Talarico et al., 1998): i) the Edixon Metamorphic Complex, ii) the Bernstein Metamorphic Complex and iii) the Gateway Hills Metamorphic Complex (Fig. 1C). The Edixon Metamorphic Complex mainly consists of micaschists and gneisses containing bands and lenses of calc-silicate rocks, with minor amphibolites in the southernmost outcrops of the range. It has been proposed that this complex underwent medium- to high-grade metamorphism and partial melting under low-P conditions and that it shows close similarities to the internal sequences of the Wilson Terrane, including migmatites and Granite Harbour Intrusive Complex granitoids (Ghiribelli, 2000; Talarico et al., 1998). However, the event and conditions of partial melting in the Wilson Terrane and in particular in the Edixon Metamorphic Complex of the Lanterman Range have not been addressed in the last two decades. The Bernstein Metamorphic Complex consists of micaschists and gneisses affected by medium- to high-grade metamorphism under intermediate-P conditions. Rare calc-silicate rocks, migmatites and granitoids are present in the complex (Ghiribelli, 2000; Talarico et al., 1998). The Gateway Hills Metamorphic Complex is characterized by abundant mafic and ultramafic rocks, including well-preserved eclogite-facies rocks, with minor gneisses and quartzites (Di Vincenzo et al., 1997, 2016; Ghiribelli et al., 2002; Palmeri et al., 2003, 2007, 2009, 2011). There are no granitoids in this complex (Talarico et al., 1998). In situ U-Pb ages on zircons from 530 to 500 Ma have been established for the eclogite formation (Di Vincenzo et al., 2016).

The evolution of the Lanterman Range (Capponi et al., 1999, 2002; Crispini et al., 2007; Di Vincenzo et al., 2014, 2016; Federico et al., 2010) can be summarized in an early subduction with a "cold" eclogite formation (530 Ma) and ongoing regional calc-alkaline magmatism, west-over-east thrusting at ca. 500 Ma with the outboard accretion of an island-arc (Bowers Terrane) onto the Gondwanan margin generating an "hotter" eclogite formation, followed by sinistral strike-slip shearing at 480–460 Ma ago, both under amphibolite to greenschist-facies metamorphism. Large amplitude folding of the late Ross or Lachlan orogens in the late Ordovician and Cenozoic brittle tectonics terminated the evolution of the suture.

2.2. Petrography and bulk composition

The studied rock belongs to the Edixon Metamorphic Complex of the Lanterman Range, was sampled south-east of Mt. Edixon (71° 50′ 23.597"S, 163°39′41.35″E) and stored in the PNRA (Programma Nazionale Ricerche in Antartide) rock repository at the Museo Nazionale dell'Antartide (Siena, Italy) as specimen 24–12-94GO5 (from hereafter GO5). The rock is a fine-grained psammitic schist composed of biotite, muscovite, quartz, plagioclase, garnet, K-feldspar, minor apatite and tourmaline (Fig. 2), and virtually free of Al_2SiO_5 polymorphs. Muscovite and biotite are abundant and define a well-developed planar foliation. They occur as mm-sized crystals with very little internal deformation, straight boundaries and no evidence of alteration (Fig. 2A, B). Quartz is abundant and occurs in coarse crystals or tiny aggregates of subgrains with segmented borders showing evidence of bulging. Garnet is scarce, with average diameter < 400 μm and exceptionally up to $\approx$1 mm. The rock displays evidence for extensive retrograde replacement of garnet by biotite (Fig. 2C, D). The relicts of garnet contain inclusions, mostly of former melt and fluid (see below), more rarely of biotite and very small rutile, and exceptionally of probable sillimanite (Fig. 2C–F). The latter has been observed only as needles of fibrolite in one crystal of garnet (Fig. 2F, G). Sillimanite, rutile, ilmenite and graphite have not been detected in the rock matrix. Overall, the mineralogical composition and texture of the studied rock would suggest a medium grade metapsammite. This inference is supported also by the absence of microstructures indicating the former presence of melt, such as grains with euhedral crystal faces or pseudomorphs after melt films (e.g., Holness et al., 2011). However, the occurrence of melt inclusions in garnet (Fig. 3A, B) demonstrates the contrary, i.e., that the rock spent part of its evolution at suprasolidus conditions, with the growth of peritectic garnet that could include rare crystals of sillimanite along with melt droplets. Given the rarity of sillimanite in the rock, it is plausible that anatexis took place at (or just after) the very beginning of growth of this phase. Otherwise one would expect much more abundant inclusions of Al_2SiO_5 in garnet and also associated with melt inclusions, as, for example, in the anatectic migmatites form Jubrique (Acosta-Vigil et al., 2016; Bartoli et al., 2014) where kyanite is often trapped in melt inclusions. The anatectic event was followed by an extensive, almost complete, recrystallization of the rock at lower temperatures, with resorption of garnet and development of the pervasive Bt-Ms foliation (mineral abbreviations after Whitney and Evans, 2010).

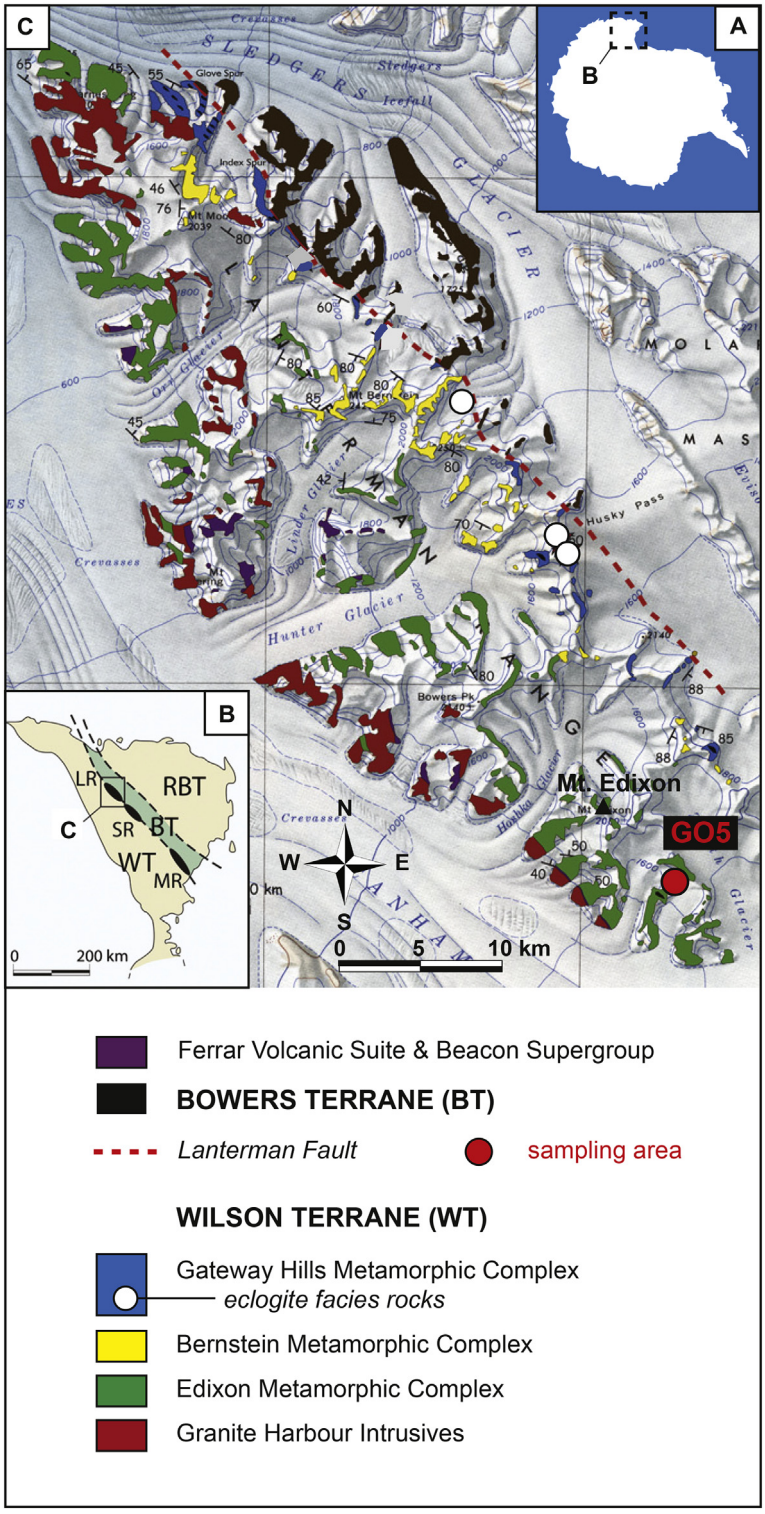

Fig. 1. A) Antarctica and location of the northern Victoria Land; B) northern Victoria Land and its main localities, RBT, Robertson Bay Terrane; BT, Bowers Terrane (green field); WT, Wilson Terrane; LR, Lanterman Range; SR, Salamander Range; MR, Mountaineer Range; C) geological map of the Lanterman Range (after Ghiribelli, 2000) and location of the sampling area. The Lanterman Fault is the northern zone of the Lanterman-Mariner suture.

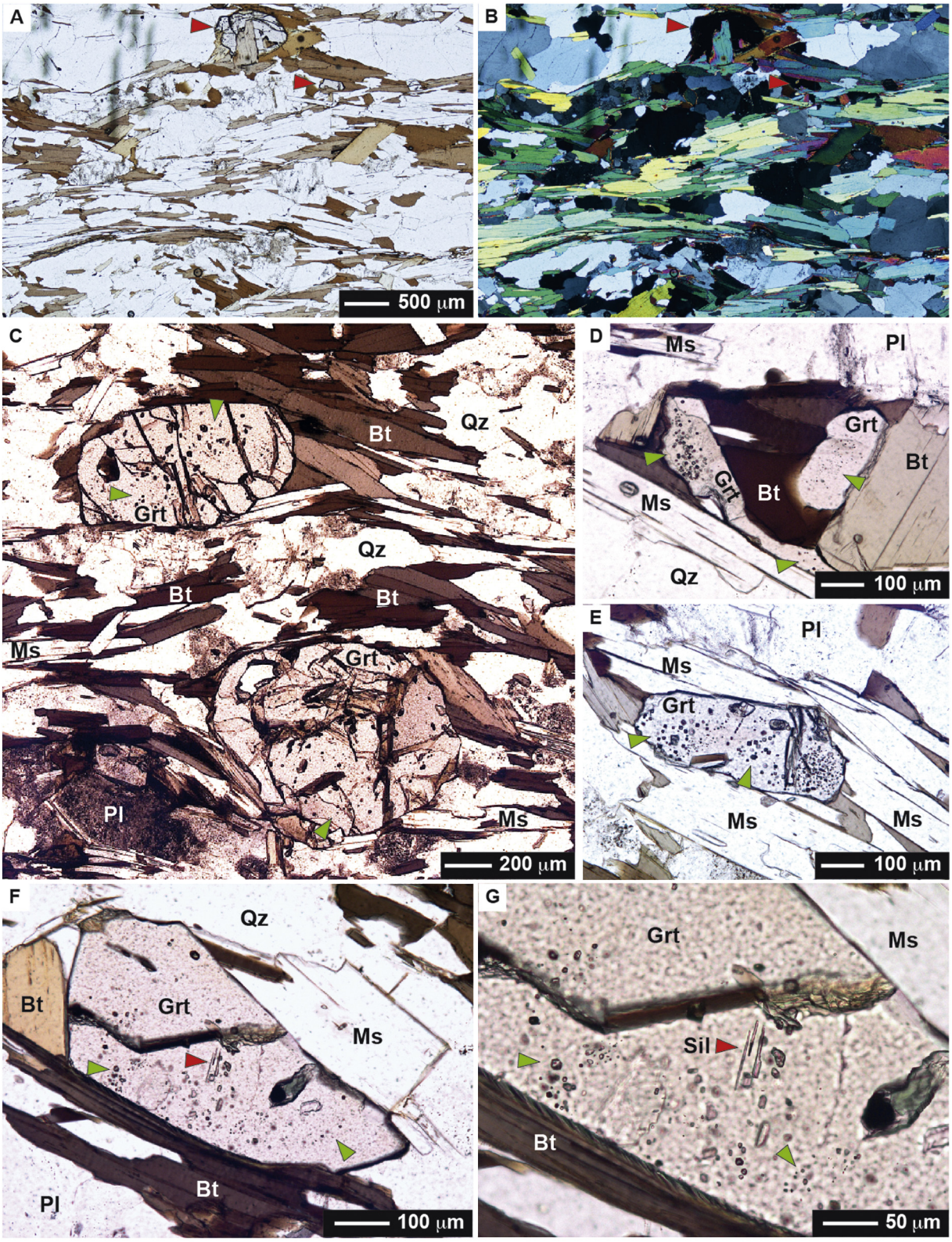

Fig. 2. Photomicrographs of sample GO5 under optical microscope. Green arrows locate clusters of MI and FI. (A, B) General appearance of the sample, with rare, resorbed garnet crystals (red arrows) in a strongly foliated matrix of muscovite and biotite, plagioclase and quartz. The micas display straight, well-equilibrated boundaries and very little bending and internal deformation. A: plane polarized light (PPL); B: crossed polarizers. (C) The two largest and best preserved crystals of garnet in the thin section. Replacement by biotite is scarce, and inclusions are located throughout the upper crystal and at the rim of the lower one. PPL. (D) A relict garnet almost completely replaced by biotite, preserves abundant FI and MI. PPL. (E) A resorbed crystal of garnet, wrapped by the Ms + Bt foliation, contains abundant negative crystal inclusions. Muscovite consists of well-equilibrated, undeformed lamellae. PPL. (F) Relict garnet with clusters of inclusions also contains needles of sillimanite (red arrow). PPL. (G) Close-up view of (F), highlighting the sillimanite needles enclosed in the garnet together with negative crystal shaped inclusions. PPL.

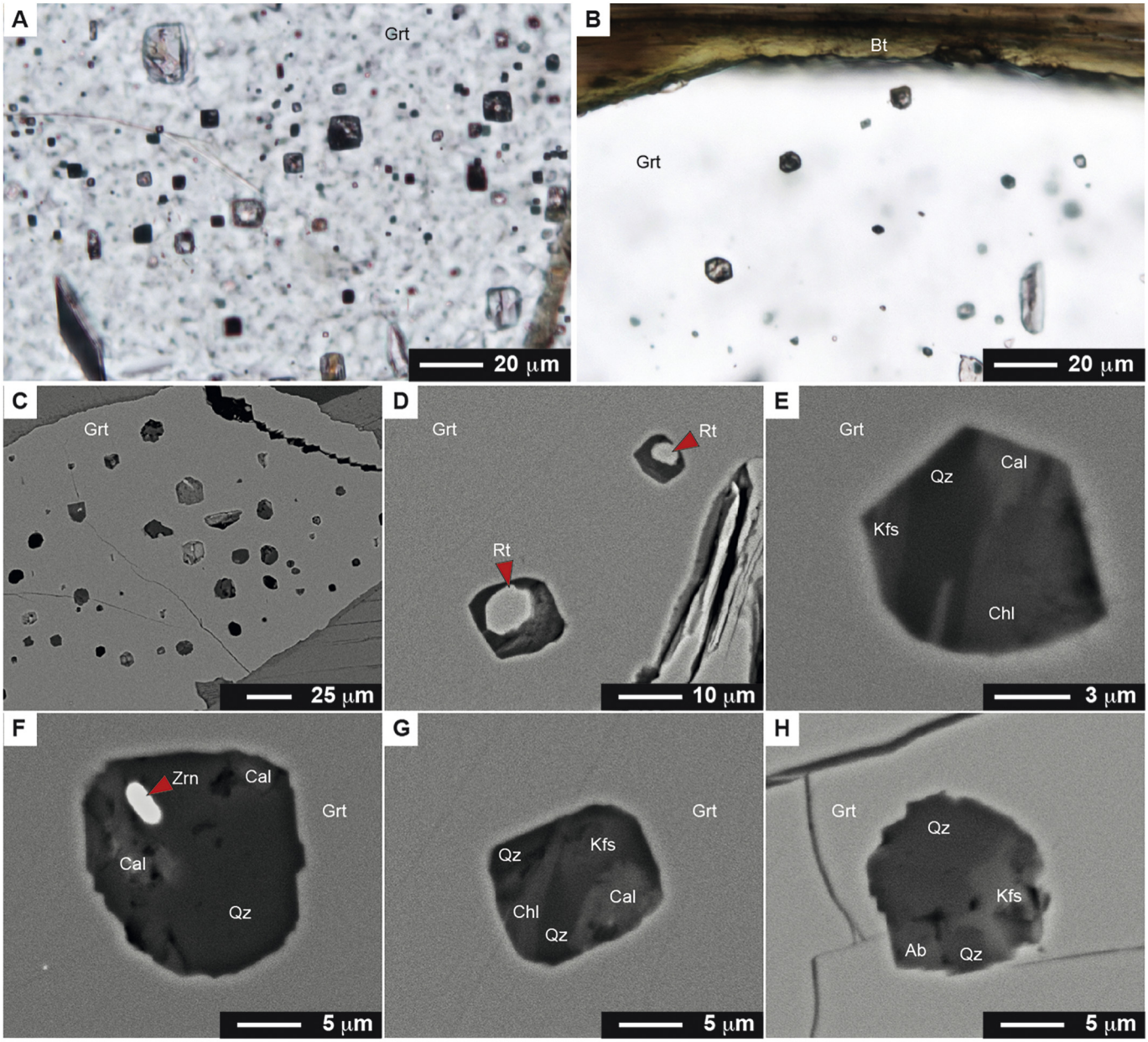

Fig. 3. Fluid and melt inclusions in the garnets from sample GO5. (A, B) Optical (PPL) images of inclusions displaying a well-developed negative crystal shape. The polycrystalline nature is apparent even under optical observation. (C–H) SEM backscattered images of inclusions. (C) General appearance of a cluster of FI and MI. Some inclusions are empty (black) because of fluid loss and/or mechanical removal of solids in them. (D) Two MI containing trapped rutile (red arrows). (*E*-H) Examples of the occurrence of nanogranitoids in the studied sample. Some inclusions have a well developed negative crystal shape (E, G) whereas others are more irregular, stepped outline (F, H). Calcite is frequently detected (E-G), along with chlorite (E, G). Trapped zircon can also be present (red arrow in F).

3. Methods

3.1. Analytical techniques

After MI recognition by optical microscopy, the mineral phases and the inclusions were first characterized in detail on polished thin sections by back-scattered electron images (BSEs) obtained with FESEM Sigma Zeiss at the ICMATE - CNR of Padova and with SEM CamScan MX3000 at the Department of Geoscience of the University of Padova.

The mineral phases and the glass of the inclusions were investigated by Micro-Raman spectroscopy using the HORIBA Jobin Yvon LabRAM HR 800 located at the Institute of Geosciences, University of Potsdam. The machine is equipped with a Peltier-cooled multichannel CCD detector and coupled with an Olympus BX41 petrographic microscope. An air-cooled NdYAG laser was used for excitation ($\lambda = 532$ nm, laser power on the sample of 2–3 mW) with a grating of 300 lines/mm, slit width and confocal hole set to 100 and 200 μm, respectively. The Raman spectra of the solid and fluid phases were acquired with a 100× objective lens in the wavenumber range 100–4000 cm^{-1}, integrating 3 repetitions of 60 s with spectral resolution of 10 cm^{-1}.

The composition of mineral phases and glasses was determined using a JEOL JXA 8200 Superprobe at the Dipartimento di Scienze della Terra, Università di Milano (Italy) using natural and synthetic silicates and oxides as standards. Analytical parameters for minerals were beam diameter of 3 μm, 15 kV accelerating voltage, 5 nA current, counting time of 30 s on peak and 10 s on background. For glass analyses, the beam diameter was reduced to 1 μm and the counting time to 10 s on peak and 2 s on background. Sodium, K, Al, and Si were the

first analyzed elements to limit element loss. Concentrations were corrected against leucogranitic glass standards with comparable H_2O contents (Morgan and London, 2005). Details concerning the application of correction factors and the composition of the standard glasses are given by Ferrero et al. (2012) and Bartoli et al. (2013a, 2013b).

The analysis of H and C in glasses was performed using the Cameca Nano Secondary Ion Mass Spectrometry 50 (NanoSIMS) installed at Muséum National d'Histoire Naturelle in Paris (France). Polished experimental capsules with MI exposed on the garnet surface and standard glasses were mounted in Indium (Aubaud et al., 2007). MI were identified by collecting secondary ion images of Si, K and Fe. For every analysis, we first performed a pre-sputtering step on a $3 \times 3\ \mu m^2$ surface area for 2 min with a 400 pA primary Cs^+ beam to remove gold coating, surface contamination and reach a steady-state sputtering regime. Then a primary beam of 37 pA was used for data acquisition. Data were acquired by rastering a $3 \times 3\ \mu m^2$ surface area and collecting only ions from the inner $1 \times 1\ \mu m^2$ (beam blanking mode) to reduce surface contamination. Each analysis stacked about 200 cycles, each cycle being 1.024 s long. The $^6OH^-$ (used as a proxy for H_2O), $^{28}Si^-$, $^{39}K^{16}O^-$ and $^{56}Fe^{16}O^-$ were recorded simultaneously in multicollection mode. We checked that $^{16}OH^-/^{28}Si^-$ ratio was stable during MI analyses (see Supplementary Table S1). Secondary ions were collected by electron multipliers with a dead time of 44 ns. Mass resolution was set to 10,000. One inclusion was large enough for replicated analyses. For NanoSIMS calibration we used a 5.5 wt% H_2O-bearing leucogranitic glass from Acosta-Vigil et al. (2003), a 4.3 wt% H_2O- bearing leucogranitic glass from Behrens and Jantos (2001) and an anhydrous leucogranitic glass from Morgan and London (2005). The standards used for the determination of CO_2 contents were four trachyandesitic standards (STR 9, 10, 11 and 13) from the Stromboli volcano experimentally doped in carbon and water by Bureau et al. (2003). H and C concentrations were recalculated as H_2O and CO_2, respectively. Data corrections, using the aforementioned calibration, and error calculations were performed using the R program following the procedure described in Bartoli et al. (2014) and Thomen et al. (2014). During the session, the vacuum in the analysis chamber remained between 2.5 and 5×10^{-10} Torr.

3.2. Remelting of inclusions

The 'remelted' inclusions are those in which the crystalline assemblage was completely melted to a single glassy phase, but melt + vapor homogenization was not achieved. Experimental remelting of the melt inclusions was performed on hand-picked separates of garnets obtained from crushed rock pieces sieved at <500 μm size. The garnet fragments were loaded into Au capsules filled with dry powder of silica or chemically pure $CaCO_3$. The capsules were loaded in a salt + MgO + graphite assembly and experiments were performed in single stage piston cylinder apparatus at the Department of Geosciences of the University of Milan at condition from 740 °C to 900 °C at 0.8 and 1.0 GPa, with duration of 21–68 h (Table 1). The confining pressures approximate the metamorphic conditions as estimated by thermodynamic phase equilibria to prevent decrepitation of polycrystalline inclusions during remelting. The temperature was controlled by a K-type thermocouple with uncertainty of ±5 °C. To avoid decrepitation of inclusions, quenching was performed at experimental pressure and load was released after achieving ambient temperature (see details in Bartoli et al., 2013a). After the experiments, the capsules containing garnet + SiO_2 were mounted in epoxy and polished to expose inclusions, whereas the capsules containing garnet + $CaCO_3$ were first opened and immersed in diluted HCl to dissolve calcite and recover the garnet grains. The garnet grains were mounted in epoxy and polished (more experimental details in Bartoli et al., 2013a and Ferrero et al., 2015).

Table 1
Experimental conditions of piston-cylinder remelting experiments.

#	matrix	T (°C)	P (GPa)	time (hrs)
ANT7	$CaCO_3$	740	0.8	46
ANT9	$CaCO_3$ and SiO_2	760	1.0	48
ANT8	SiO_2	780	0.8	68
ANT10	SiO_2	780	1.0	67
ANT5	$CaCO_3$	810	0.8	23
ANT3	$CaCO_3$	850	0.8	22
ANT4	$CaCO_3$	900	0.8	21

3.3. Thermodynamic modelling

Phase equilibria calculations were done in the model chemical system MnNCaKFMASHT using the Perple_X software (Connolly, 2009) with the thermodynamic database of Holland and Powell (2003 revision). We used the solution models of White et al. (2007) for melt, Holland and Powell (1998) for garnet, Tajčmanová et al. (2009) for biotite, Coggon and Holland (2002) for white mica, Newton et al. (1980) for plagioclase, and Thompson and Hovis (1979) for K-feldspar. The bulk composition of the rock was obtained from XRF analysis. As it does not show a residual character and may be considered representative of the original protolith, there is no necessity of melt reintegration (see Bartoli, 2017, Bartoli et al., 2019). This is also supported by the absence of pseudomorphs after melt films, with melt inclusions being the only petrographic evidence of past anatexis of the rock. The amount of H_2O used in the calculation was assumed to be the loss on ignition (L.O.I.) from the XRF analysis (=1.5 wt%).

4. Results

4.1. Microstructures of melt and fluid inclusions

The inclusions preserved in the starting material and those recovered after remelting experiments were characterized on the basis of optical microscopy, BSE imaging, EDS elemental mapping and micro-Raman spectroscopy, and distinguished in fluid (FI) and (former) melt (MI), the latter also called nanogranitoids (Cesare et al., 2015). By MI we indicate both the polycrystalline nanogranitoids before experiments, and the product of their experimental remelting to a glass.

In the garnet relicts preserved from extensive resorption, inclusions may in places show irregular distribution, in other tend to cluster at the rims of large crystals, or in other are located in the core of tiny crystals (Fig. 2C–F). Despite the inability to reconstruct the exact textural position of inclusions in the garnet, the clustering of inclusions is nonetheless indicative of a primary entrapment (according to Roedder, 1984), and suggest that inclusions were trapped throughout the entire garnet growth. In the garnet, inclusions consist of both FI and MI coexisting in the clusters (Fig. 3A, B), suggesting that they belong to the same fluid/melt inclusion assemblage and that entrapment took place during garnet growth in a condition of fluid-melt immiscibility.

Most FI and MI are <10 μm in diameter, have isometric (negative crystal) shapes, are equally abundant and have comparable size range (Fig. 3). In MI, typical phases are albite, K-feldspar, quartz, muscovite, biotite, chlorite, calcite, rare siderite and rare trapped rutile. Phase equilibria modelling demonstrated that the formation of chlorite does not require the infiltration of external fluids; rather, chlorite can form in the subsolidus during cooling (Bartoli et al., 2019). The FI contain a C-O-H fluid composed of H_2O and CO_2 (Fig. 4A), with rare CH_4, N_2, H_2S and solid calcite. The presence of H_2O is marked by the broad band between 3100 and 3600 cm^{-1}, the CO_2 by the presence of the Fermi diad (peaks at 1285 $cm^{-1}$and 1387 cm^{-1}), with peak distance (Δ) corresponding to CO_2 density of <0.1 g cm^{-1} (see Wang et al., 2011). In both MI and FI the carbonates are interpreted as step-daughter phases, as modelled by Carvalho et al. (2020).

After the experiments, the inclusions were carefully inspected to infer the temperature of entrapment from approach to remelting equilibrium (Fig. 5). At 740 °C, the MI have well defined negative crystal

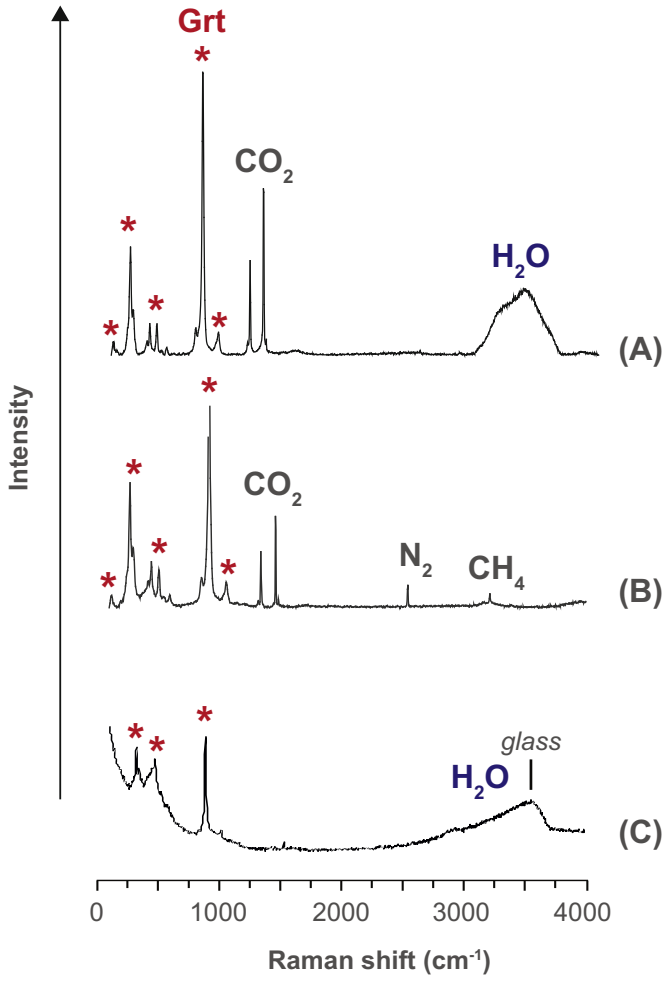

Fig. 4. Representative Raman spectra of phases and volatile species in: A) fluid inclusion; B) shrinkage bubble in remelted glass; C) remelted glass (Grt = garnet).

shapes and contain glass (yellow arrows in Fig. 5) together with abundant unmelted crystals of quartz, biotite, muscovite, albite and rutile, indicating that remelting was incomplete (i.e., they are partially remelted inclusions). At 760 °C, albite and muscovite are completely resorbed, biotite is less frequent, and quartz is still present, with a typical round shape suggesting incomplete remelting. However, some inclusions are completely remelted to a homogeneous glass, and contain a shrinkage bubble. At 780 °C experiments show a greater approach to equilibrium with >40–50% remelted inclusions, displaying regular walls, negative crystal shape and absence of offshoots. The presence of rounded unmelted quartz is rare. At 810 °C, completely or partly remelted inclusions display offshots (white arrows in Fig. 5) and the presence of secondary minerals (i.e., formed during experiments or upon quenching) as aggregates of tiny acicular Bt. Remelted inclusions represent >70% of the total. At 850 °C and 900 °C almost all inclusions are remelted but with evidence of overheating (see Acosta-Vigil et al., 2016; Bartoli et al., 2013a, 2013b; Cesare et al., 2015) as indicated by i) presence of lobate-cuspate walls at the contact with the host garnet, ii) frequent offshoots, iii) growth of secondary garnet at the inclusion walls, iv) segmented straight walls after assimilation of the Grt (at 900 °C). Rutile as trapped phases becomes less common at $T > 810$ °C and almost absent at 900 °C. In the Raman spectrum shown in Fig. 4C, the remelted glass has a broad band at ≈3500 cm^{-1} related to the presence of H_2O, while the shrinkage bubble within the glass contains a fluid mixture of $CO_2 + N_2 + CH_4$ (Fig. 4B).

4.2. Major elements composition of remelted glasses

In order to determine the composition of the melt produced during anatexis of the metapsammite, and to infer the temperature of entrapment of inclusions, we conducted EMP glass analyses on completely or partially remelted glasses to explore their potential interaction with the host garnet as function of experimental temperature (Table 2). We excluded analyses with clear signal of contamination either by minerals preserved in the inclusions or by host garnet. The difference to 100% of the totals may reflect not only the fluid content but also interaction of the microprobe beam with the shrinkage bubble if present below the polished surface of the MI (see discussion below on H_2O-CO_2 content), so results of the analyses were recalculated on anhydrous basis (100 wt%). Fig. 6 compares the recalculated anhydrous compositions of the glasses recovered in all the experiments. The average MnO vs. FeO_t content is respectively 0.6 wt% and 1.7–1.9 wt% up to 780 °C, and systematically increases up to 0.9 wt% and 3.2 wt% at 900 °C (Fig. 6A). The $FeO_t + MgO + TiO_2$ is 1.8–2.2 wt% up to 780 °C with variable amount of SiO_2 within the range 76–78 wt% at 740 °C, 72–80 wt% at 760 °C and 76–79 wt% at 780 °C (Fig. 6B). At T > 810 °C, the $FeO_t + MgO + TiO_2$ can be above 4 wt% and inversely proportional to SiO_2. The CaO vs. SiO_2 has similar behavior for most temperatures with highest CaO and lowest SiO_2 at 900 °C (Fig. 6C). No clear temperature dependence is visible on the Na_2O vs. SiO_2 plot, except at 900 °C where the SiO_2 is systematically lower for comparable Na_2O contents (Fig. 6D). With a few exceptions the glasses are peraluminous, with alumina saturation index (ASI) in the range 1.0–1.8 (Fig. 6F). Al_2O_3 is inversely proportional to SiO_2 at 760–810 °C (Fig. 6E), but values get dispersed at $T > 850$ °C resulting in a larger spread of ASI, that may be <1. The systematic variations reported in Fig. 6 may result from progressive remelting of phases in inclusions where glasses are not completely homogeneous (e.g., quartz, feldspars and micas at 740 °C; quartz at 760 °C) or melt contamination by interaction with the host garnet. The grey vectors in Fig. 6B and E point from average glass composition at 780 °C to average garnet core composition and suggests that host interaction is not negligible at T > 810 °C. As a consequence, we consider the homogeneous glass compositions obtained at 760–780 °C as most representative of the anatectic melt trapped within garnets.

In Fig. 7 the CIPW normative composition of glasses remelted at 760–780 °C is plotted on the pseudoternary normative diagrams Qz-Ab-Or and An-Ab-Or. Compositions at 760 °C include both incompletely remelted glasses coexisting with unresorbed quartz, and homogeneous remelted glasses. The MI cluster above the cotectic lines at 0.5–1.0 GPa is consistent with the displacement of cotectic lines towards Qz apex as effect of increasing Al and Ca content in the granite model system (see Bartoli et al., 2016a). The composition of MI at 760 °C differ by the lower SiO_2 which is related to the presence of incompletely remelted quartz in the inclusions. However, few homogeneous glasses at 760 °C overlap with glasses at 780 °C suggesting that melt homogenization is presumably achieved within the interval 760–780 °C and these glasses represent the closest approximation to the original anatectic melt. Displacement of the MI composition from the minimum melt in the Qz-Ab-Or model system has been explained by Wilke et al. (2017) as due to the presence of extra components in natural systems, mostly Ca, Fe and Ti. Wilke et al. (2017) report a displacement of the eutectic point to Or-enriched composition at similar Qz amount when melts have ≈3.5–7 wt% normative An. The An content of remelted glasses clusters at 7–12 wt% with few analyses up to 22–29 wt%. The MI are relatively heterogeneous in Qz/feldspar and Ab/Or ratios but without clear trends compared to those reported by Bartoli et al. (2016a) where compositional alignments of remelted granitic glasses parallel to the Qz-feldspar join were interpreted as due to slow diffusion of Si and Al compared to alkalis in granitic melts (see Acosta-Vigil et al., 2006, 2017). In the An-Ab-Or projection of Fig. 7, glass compositions plot in the granite field or close to the boundary between granite and Qz-monzonite, with some Qz-monzonite compositions. In Fig. 7, the composition of MI is

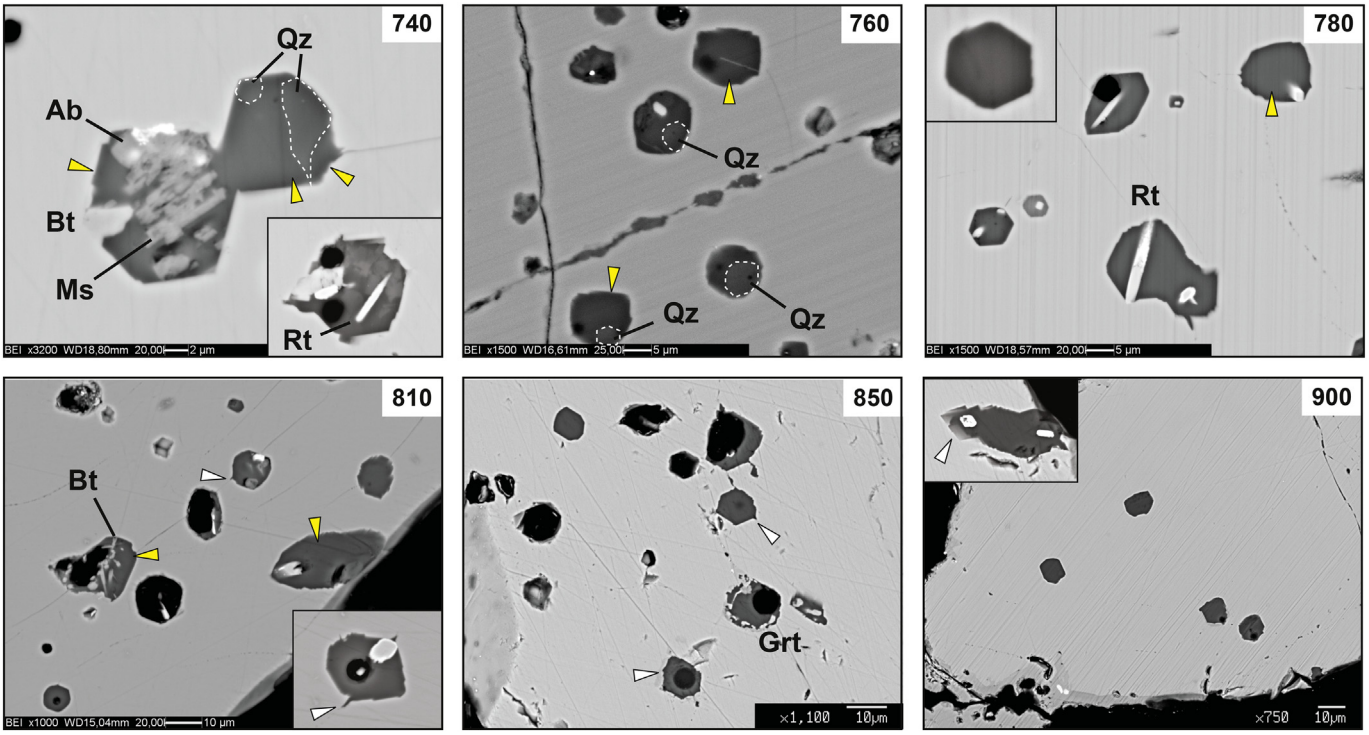

Fig. 5. Microstructures of MI under scanning electron microscope (BSE images) after remelting experiments in piston cylinder apparatus at increasing temperature: 740 °C - partially homogenized MI with glass (yellow arrows), quartz, biotite, muscovite, albite and rutile; 760 °C - glassy MI with rounded quartz (= partial resorption); 780 °C - glassy MI with regular walls, negative crystal shape and crystals of rutile; 810 °C - homogenized MI with local offshots (white arrows) and secondary acicular Bt; 850 °C - homogenized MI with lobate-cuspate walls, offshots (white arrows), and secondary Grt suggesting overheating and host interaction; 900 °C - glassy MI with segmented straight walls after assimilation of host Grt (inset).

distinct from that of MI recovered in garnet of metasediments from Ojén (Bartoli et al., 2013b, 2013c) equilibrated at 700 °C and 0.5 GPa, and in plagioclase of Grt-Bt-Sil enclaves from El Hoyazo (Acosta-Vigil et al., 2010; Bartoli et al., 2016a) equilibrated at 700–750 °C and 0.5–0.7 GPa which may reflect different P-T-X-a_{H2O} as suggested by Acosta-Vigil et al. (2017). Most of the glasses plot in the calcic field of the modified alkali-lime index (MALI = $Na_2O + K_2O - CaO$) vs. SiO_2 (wt%) after Frost et al. (2001) and in the rhyolite field of the TAS classification (Fig. 8A, B). Few glasses at 760 °C and one at 780 °C are calc-alkalic or dacitic.

4.3. Volatile content of remelted glasses

The H_2O and CO_2 concentration in glasses was determined by nanoSIMS only on MI remelted at 760 °C and 780 °C (Supplementary Table S1) and performed on selected homogeneous portion of the glass exposed on the surface of polished garnets.

The H_2O content of individual analyses is reported in Fig. 9 and is between 2.2 and 8.0 wt% at 760 °C and 3.0–6.5 wt% at 780 °C, while the corresponding CO_2 is 250–850 ppm at 760 °C and 500–2200 ppm at 780 °C. In Fig. 9B and C the MI analyses are grouped according to host Grt and display similar variability except for garnets ANT9–1 and ANT8–1 with higher scatter for H_2O and CO_2, respectively. The averages at 760 °C and 780 °C (white circles in Fig. 9A) are similar for H_2O with 4.3 ± 1.8 wt% at 760 °Cand 5.3 ± 1.0 wt% at 780 °C, but differ for CO_2 with 407 ± 184 ppm at 760 °Cand 1147 ± 519 ppm at 780 °C.

4.4. Mineral chemistry

The compositions of minerals are reported in Supplementary Table S2. Garnet is almandine-rich (≈ 57 mol% Alm) with a weak compositional zoning. From core to rim, the pyrope content decreases from 12 mol% to 8–10 mol% while grossular and spessartine components increase from 2 mol% to 4 mol%, and from 25 mol% to 28–30 mol% respectively. The almandine content is constant throughout the crystal. The slight rimward increase of Mn is consistent with a process of Mn uptake by garnet during resorption (e.g., Hollister, 1977), in agreement with the observed textures.

The white mica is potassic (X_{Ms} = 0.92–0.95) with Si ranging from 3.00 to 3.04 a.p.f.u. (atoms per formula unit) (11 oxygens), Al ranging from 2.76 to 2.72 a.p.f.u. and X_{Mg} of 0.41–0.45. The Ti content (0.03 a.p.f.u.) is typical of amphibolite-facies subsolidus muscovite (e.g., Cesare, 1999, compare with Redler et al., 2012), but it should be observed that the rock matrix does not contain a Ti saturating phase (Ilm or Rt) and therefore the Ti content of muscovite is not at maximum. The composition of the white mica is similar to that reported by Di Vincenzo et al. (2001) in sample BT5 and BT2 collected from the Edixon and Bernstein Metamorphic Complexes respectively and classified by the Authors as type-2 muscovite with selected area diffraction (SAED) pattern of 2 M1 polytypes.

Biotite shows no systematic variations with microstructural occurrence, and has a fairly constant composition, with Ti of 0.11–0.13 a.p.f.u. and X_{Mg} of 0.44–0.45. Also for biotite, the low titanium content is typical of amphibolite-facies subsolidus conditions (Tajčmanová et al., 2009), but is not at the maximum possible values due to the lack of a Ti-saturating phase in the rock. Plagioclase composition has 15–23 mol% anorthite, 76–84 mol% albite and ca. 1 mol% K-feldspar. Alkali feldspar is almost pure K-feldspar with albite <1–3 mol%.

4.5. Thermodynamic modelling

A phase diagram for the specific bulk composition (i.e., pseudosection) of the studied sample was calculated by phase equilibria modelling with the aim of constraining the P-T conditions of

Table 2
Major element composition (wt%) of glasses in remelted inclusions on anhydrous basis with averages. Numbers in parentheses refer to 1σ standard deviation.

Temp.	740 °C			*Mean*	*[c]STD*	760 °C											*Mean*	*[c]STD*
SiO_2	77.60	76.20	78.05	*77.28*	*(0.97)*	80.09	73.53	75.18	76.25	76.36	73.21	73.22	75.63	72.47	72.95	72.53	*74.67*	*(2.32)*
TiO_2	0.02	0.03	0.00	*0.02*	*(0.02)*	0.07	0.10	0.06	0.04	0.01	0.00	0.03	0.15	0.11	0.14	0.38	*0.10*	*(0.10)*
Al_2O_3	13.95	14.56	13.89	*14.13*	*(0.37)*	11.33	16.25	14.54	15.16	14.68	15.32	14.28	13.93	14.78	14.68	14.73	*14.52*	*(1.22)*
FeO	1.55	2.05	1.56	*1.72*	*(0.28)*	1.57	1.36	1.45	1.23	1.45	1.53	2.57	1.57	1.89	1.75	2.09	*1.68*	*(0.38)*
MnO	0.53	0.84	0.52	*0.63*	*(0.18)*	0.69	0.38	0.59	0.66	0.70	0.31	1.13	0.65	0.39	0.41	0.52	*0.58*	*(0.23)*
MgO	0.14	0.16	0.05	*0.12*	*(0.06)*	0.06	0.09	0.07	0.06	0.06	0.16	0.16	0.08	0.17	0.18	0.06	*0.10*	*(0.05)*
CaO	1.02	0.56	1.00	*0.86*	*(0.26)*	0.72	2.62	1.22	1.25	1.20	3.11	1.15	0.81	3.33	3.41	3.74	*2.05*	*(1.18)*
Na_2O	1.91	3.32	3.03	*2.75*	*(0.74)*	2.24	2.35	2.59	1.19	1.32	1.78	2.70	2.86	2.78	2.75	1.92	*2.23*	*(0.59)*
K_2O	3.26	2.29	1.90	*2.48*	*(0.70)*	3.25	3.33	4.31	4.16	4.22	4.57	4.75	4.33	4.08	3.74	4.03	*4.07*	*(0.47)*
Total	100.00	100.00	100.00			100.00	100.00	100.00	100.00	100.00	100.00	100.00	100.00	100.00	100.00	100.00		
[a]$Total_{EMPA}$	85.07	86.84	85.18	*85.70*	*(0.99)*	82.84	87.12	87.89	86.16	85.73	87.15	88.68	85.73	89.90	91.43	88.83	*87.41*	*(2.34)*
[b]H_2O(diff)	14.93	13.16	14.82	*14.30*	*(0.99)*	12.88	12.88	12.11	13.84	14.27	12.85	11.32	14.27	10.10	8.57	11.17	*12.20*	*(1.79)*
ASI	1.64	1.63	1.57	*1.61*	*(0.04)*	1.33	1.33	1.31	1.74	1.65	1.13	1.22	1.28	0.98	0.99	1.03	*1.27*	*(0.25)*
AI	0.07	0.06	0.07	*0.07*	*(0.00)*	0.04	0.09	0.06	0.09	0.08	0.07	0.05	0.04	0.06	0.06	0.07	*0.06*	*(0.02)*
MALI	4.15	5.05	3.93	*4.38*	*(0.59)*	4.77	3.07	5.68	4.10	4.34	3.25	6.30	6.38	3.53	3.07	2.22	*4.25*	*(1.40)*

Temp.	780 °C																		*Mean*	*[c]STD*
SiO_2	78.58	77.97	77.97	78.29	76.34	76.09	75.80	77.81	78.38	75.56	78.74	77.02	78.44	78.11	77.09	78.16	77.48	76.82	*77.48*	*(1.00)*
TiO_2	0.00	0.07	0.05	0.01	0.23	0.00	0.05	0.00	0.11	0.33	0.02	0.00	0.18	0.15	0.22	0.21	0.07	0.05	*0.10*	*(0.10)*
Al_2O_3	12.97	12.91	13.47	13.06	14.24	13.58	13.35	12.77	13.02	13.21	12.81	13.41	12.67	12.91	13.48	13.00	13.48	13.68	*13.22*	*(0.40)*
FeO	2.19	1.91	1.95	1.96	1.92	2.16	1.74	1.97	1.87	1.90	2.17	1.96	1.68	1.74	1.76	1.44	1.83	2.46	*1.92*	*(0.23)*
MnO	0.53	0.59	0.70	0.56	0.44	0.59	0.66	0.63	0.72	0.59	0.62	0.49	0.59	0.63	0.40	0.69	0.58	0.73	*0.60*	*(0.09)*
MgO	0.22	0.17	0.11	0.14	0.12	0.22	0.71	0.14	0.18	0.13	0.18	0.29	0.09	0.09	0.11	0.08	0.12	0.27	*0.19*	*(0.14)*
CaO	0.85	0.41	0.84	0.56	1.92	2.45	2.36	1.28	1.09	2.94	0.90	0.93	0.74	0.72	0.81	0.90	1.26	1.40	*1.24*	*(0.71)*
Na_2O	1.53	1.95	1.48	1.75	1.57	1.44	1.58	1.58	1.92	1.48	1.67	2.03	1.68	1.77	2.19	2.48	2.16	2.60	*1.83*	*(0.35)*
K_2O	3.13	4.01	3.44	3.67	3.23	3.47	3.75	3.82	2.70	3.84	2.88	3.87	3.92	3.89	3.94	3.05	3.02	2.01	*3.42*	*(0.54)*
Total	100.00	100.00	100.00	100.00	100.00	100.00	100.00	100.00	100.00	100.00	100.00	100.00	100.00	100.00	100.00	100.00	100.00	100.00		
[a]$Total_{EMPA}$	87.54	89.54	87.64	88.81	88.10	88.93	90.18	89.98	88.59	89.77	87.04	90.36	89.46	89.90	90.66	89.79	86.76	88.32	*88.97*	*(1.18)*
[b]H_2O(diff)	12.46	10.46	12.36	11.19	11.90	11.07	9.82	10.02	11.41	10.23	12.96	9.64	10.54	10.10	9.34	10.21	13.24	11.68	*11.03*	*(1.18)*
ASI	1.74	1.56	1.75	1.66	1.49	1.28	1.22	1.41	1.61	1.11	1.70	1.46	1.52	1.53	1.44	1.44	1.48	1.52	*1.50*	*(0.17)*
AI	0.07	0.05	0.07	0.06	0.08	0.07	0.07	0.06	0.07	0.06	0.07	0.06	0.06	0.06	0.06	0.06	0.07	0.07	*0.06*	*(0.01)*
MALI	3.80	5.56	4.07	4.87	2.88	2.45	2.96	4.12	3.53	2.39	3.65	4.97	4.86	4.95	5.32	4.63	3.92	3.21	*4.01*	*(0.98)*

Temp.	810 °C															*Mean*	*[c]STD*
SiO_2	77.88	72.06	77.39	73.23	72.89	75.65	76.91	76.91	78.15	74.57	76.07	78.44	71.93	75.89	73.87	*75.46*	*(2.23)*
TiO_2	0.06	0.00	0.18	0.00	0.17	0.00	0.44	0.07	0.00	0.09	0.03	0.00	0.11	0.00	0.00	*0.08*	*(0.12)*
Al_2O_3	12.15	14.97	14.57	15.56	13.90	13.60	13.01	12.41	12.71	14.51	13.77	12.34	14.67	11.89	13.34	*13.56*	*(1.13)*
FeO	1.99	4.44	1.53	1.88	3.13	2.38	2.56	2.36	1.85	3.22	1.83	2.54	2.69	3.24	3.87	*2.63*	*(0.82)*
MnO	0.64	1.28	0.58	0.46	0.66	0.55	1.03	0.67	0.64	1.57	0.70	0.55	0.89	0.76	1.18	*0.81*	*(0.32)*
MgO	0.08	0.39	0.09	0.34	0.35	0.13	0.16	0.16	0.12	0.28	0.15	0.14	0.27	0.19	0.19	*0.20*	*(0.10)*
CaO	1.08	1.10	0.57	1.90	2.73	1.13	0.96	1.39	0.52	0.50	1.85	0.77	1.41	1.06	1.61	*1.24*	*(0.61)*
Na_2O	2.22	2.01	3.07	1.77	2.14	2.48	1.65	1.32	1.97	1.34	1.90	2.42	2.78	2.19	2.64	*2.13*	*(0.50)*
K_2O	3.90	3.75	2.02	4.87	4.02	4.08	3.29	4.71	4.05	3.90	3.71	2.78	5.24	4.79	3.29	*3.89*	*(0.84)*
Total	100.00	100.00	100.00	100.00	100.00	100.00	100.00	100.00	100.00	100.00	100.00	100.00	100.00	100.00	100.00		
[a]$Total_{EMPA}$	89.38	91.30	87.72	89.41	89.69	89.48	87.52	89.10	89.43	87.80	89.24	91.04	92.18	93.62	91.77	*89.91*	*(1.75)*
[b]H_2O(diff)	10.62	8.70	12.28	10.59	10.31	10.52	12.48	10.90	10.57	11.57	10.76	8.96	7.82	6.38	8.23	*10.05*	*(1.70)*
ASI	1.23	1.60	1.76	1.34	1.08	1.29	1.62	1.27	1.48	1.98	1.31	1.47	1.15	1.11	1.23	*1.39*	*(0.26)*
AI	0.04	0.07	0.07	0.07	0.06	0.05	0.07	0.05	0.05	0.08	0.07	0.05	0.04	0.03	0.05	*0.06*	*(0.01)*
MALI	5.04	4.66	4.52	4.74	3.43	5.44	3.98	4.65	5.50	4.75	3.76	4.44	6.61	5.92	4.32	*4.78*	*(0.83)*

Temp.	850 °C									*Mean*	*[c]STD*
SiO_2	74.90	73.40	75.60	77.01	76.32	76.96	71.98	80.78	69.50	*75.16*	*(3.26)*
TiO_2	0.30	0.30	0.05	0.19	0.03	0.21	0.36	0.38	0.11	*0.21*	*(0.13)*
Al_2O_3	12.72	15.04	13.01	13.96	13.20	14.12	14.98	11.02	15.21	*13.69*	*(1.36)*
FeO	1.99	2.10	2.46	1.74	2.47	1.90	3.43	2.21	6.00	*2.70*	*(1.33)*
MnO	0.41	0.57	0.71	0.43	0.37	0.34	0.92	0.67	1.12	*0.62*	*(0.27)*
MgO	0.12	0.28	0.19	0.22	0.23	0.25	0.34	0.26	0.65	*0.28*	*(0.15)*
CaO	2.13	2.26	1.86	0.66	2.44	0.90	3.40	0.57	1.67	*1.77*	*(0.93)*
Na_2O	2.43	2.52	1.31	4.48	1.80	3.49	2.04	0.93	2.91	*2.43*	*(1.10)*
K_2O	5.00	3.52	4.81	1.31	3.15	1.84	2.55	3.19	2.84	*3.13*	*(1.22)*
Total	100.00	100.00	100.00	100.00	100.00	100.00	100.00	100.00	100.00		
[a]$Total_{EMPA}$	92.30	88.89	89.05	90.21	88.66	87.43	89.20	76.90	89.38	*88.00*	*(4.37)*
[b]H_2O(diff)	7.70	11.11	10.95	9.79	11.34	12.57	10.80	10.80	10.62	*10.63*	*(1.32)*
ASI	0.96	1.25	1.21	1.40	1.22	1.51	1.22	1.84	1.40	*1.33*	*(0.25)*
AI	0.03	0.07	0.06	0.05	0.07	0.06	0.09	0.06	0.07	*0.06*	*(0.02)*
MALI	5.30	3.78	4.25	5.13	2.52	4.42	1.19	3.55	4.08	*3.80*	*(1.29)*

Temp.	900 °C									*Mean*	*[c]STD*
SiO_2	80.52	65.37	78.31	74.37	76.55	70.11	70.40	78.53	78.03	68.18	*74.04*	*(5.17)*
TiO_2	0.01	1.19	0.04	0.03	0.00	0.00	0.01	0.00	0.00	3.87	*0.52*	*(1.24)*
Al_2O_3	12.16	15.27	12.51	14.64	13.66	14.63	14.69	11.99	12.59	12.55	*13.47*	*(1.24)*

(continued on next page)

Table 2 (*continued*)

Temp.	900 °C										*Mean*	[c]*STD*
FeO	2.29	6.13	2.85	2.24	3.05	2.01	1.99	3.17	2.63	6.06	*3.24*	*(1.56)*
MnO	0.58	1.28	0.82	0.45	0.69	1.02	1.05	0.88	0.66	1.15	*0.86*	*(0.27)*
MgO	0.14	0.41	0.22	0.36	0.16	0.07	0.07	0.23	0.25	0.20	*0.21*	*(0.11)*
CaO	0.66	3.68	1.32	1.35	0.92	5.68	5.53	1.45	1.12	1.66	*2.34*	*(1.91)*
Na_2O	1.97	3.14	0.66	0.77	4.33	1.76	1.62	0.64	1.29	2.43	*1.86*	*(1.18)*
K_2O	1.68	3.53	3.27	5.80	0.64	4.74	4.64	3.11	3.43	3.89	*3.47*	*(1.49)*
Total	100.00	100.00	100.00	100.00	100.00	100.00	100.00	100.00	100.00	100.00		
[a]$Total_{EMPA}$	87.07	87.43	86.90	90.62	91.17	91.98	92.07	83.39	86.79	89.56	*88.70*	*(2.83)*
[b]H_2O(diff)	12.93	12.57	13.10	9.38	8.83	8.02	7.93	7.93	13.21	10.44	*10.44*	*(2.30)*
ASI	1.94	0.97	1.78	1.47	1.44	0.80	0.83	1.70	1.60	1.12	*1.36*	*(0.41)*
AI	0.07	0.06	0.08	0.07	0.06	0.06	0.07	0.07	0.07	0.04	*0.07*	*(0.01)*
MALI	2.98	2.99	2.61	5.22	4.04	0.82	0.73	2.30	3.60	4.66	*3.00*	*(1.48)*

[a] Totals from EMPA.
[b] H_2O by difference to 100%.
[c] Standard deviation.

melting and inclusions entrapment, and is reported in Fig. 10. The modelled chemical composition is reported as inset in the same figure. The presence of $CO_2 + H_2O \pm$ carbonates in MI (calcite and siderite) and FI (calcite) point to a C-O-H fluid coexisting with the rock and melt during anatexis, but owing to the difficulty of modelling the behavior of C-O-H fluids in the suprasolidus region (Bartoli et al., 2016b), an acqueous fluid ($a_{H2O} = 1$) was considered present. Slight variations in H_2O activity (tested from 0.8 to 1.0 but not reported here) resulted in limited displacement of the solidus at $P > 0.5$ GPa (Bartoli et al., 2016b), where the reaction slope is high and positive (Fig. 10).

The major phase changes highlighted in the pseudosection are the Liq-in curve of first melt appearance, almost subvertical at about 690–710 °C, and the Ms-out curve coinciding with the appearance of an Al_2SiO_5 polimorph in the assemblage. This curve has a positive slope and crosses at about 690 °C, 0.5 GPa and 830 °C, 1.5 GPa. Between the two curves are located a number of fields where melt coexists with muscovite and garnet.

Unfortunately, given the extensive retrograde reequilibration of the sample, the calculated phase diagram is unable to provide reliable constraints on the P-T conditions at which anatexis took place. The petrographic study suggests that the peak mineral assemblage is Bt + Ms + Pl + Kf + Grt + Qz + Liq ± Sil ± Rt coexisting with excess C-O-H fluid as indicated by the presence of FI and MI within the same cluster. In the pseudosection of Fig. 10, such an assemblage is not observed, Ms and Al_2SiO_5 being mutually exclusive, and Rt being stable either in the subsolidus or at $T > 800$ °C.

As the phase diagram cannot help constraining the suprasolidus history of the studied rock, we will utilize an alternative approach using the results of experimental remelting (see Section 5.1).

5. Discussion

5.1. Conditions of MI entrapment

The present study is an example of successful remelting of inclusions that adds to previous case studies of metasedimentary rocks undergoing anatexis (e.g., Cesare et al., 2015; Bartoli et al., 2016a; Tacchetto et al., 2019; Carvalho et al., 2019; Bartoli and Cesare, 2020). Previous works report MI entrapped under fluid present (Bartoli et al., 2013b; Carvalho et al., 2019, 2020) or fluid-absent melting of felsic (e.g., Cesare et al., 2015) or ultramafic rocks (Ferrero et al., 2018), and in a range of temperatures from upper-amphibolite to UHT conditions. All previous studies from metasedimentary rocks relate to Al_2SiO_5-bearing protoliths. The present research yields new data on the onset of low-T anatexis of metasedimentary crust under possibly fluid-present conditions, which are likely to be more common than previously thought (see Carvalho et al., 2019, 2020 and discussion therein). In addition, this work expands the existing database of natural melt compositions to include the liquids produced by Al_2SiO_5-free rocks comparable to metagreywackes.

The P-T-fluid conditions of melt entrapment within the host mineral can be reconstructed combining the microstructures produced during remelting experiments at increasing temperature with the proportion of remelted inclusions, the compositional variation of major elements in glass and the thermodynamic modelling. In remelting experiments, microstructural changes include i) type of minerals coexisting with glass (relict unmelted minerals, daughter minerals and trapped phases), ii) presence of offshoots (suggesting decrepitation), iii) presence of irregular boundaries between MI and Grt (indicative of host interaction), iv) crystallization of new phases (indicative of overheating), v) appearance of zoning/growth structures (indicative of intense host interaction). Since glasses remelted at 780° are mostly free of daughter minerals, have no visible cracks/offshoots, and display limited or no chemical interaction with the host garnet (e.g., low MnO vs. FeO_t in Fig. 6A), they can be confidently interpreted as representative of entrapment conditions. However, at 760 °C, where most inclusions still contain quartz which has not been completely re-homogenized and hence lower SiO_2 melts, few remelted inclusions resemble in texture and composition those typically recovered at 780 °C. Remelted inclusions have not been observed at 740 °C while above 810 °C they display evidence of intense glass-host interaction. So it is reasonable to conclude that the interval 760–780 °C best approximates the entrapment temperatures. This inference is key to interpret the results of thermodynamic modelling.

In Fig. 10, considering that modelling of Ti-rich phases (Rt-Ilm) suffers from problems and uncertainties related to available thermodynamic properties and *a-x* models for Ti-bearing end-members, and considering that the rare sillimanite observed suggests that the rock equilibrated very close to a Sil-in equlibrium, it may be inferred that the field that best approximates the peak equilibrium conditions should be the Bt-Ms-Pl-Kfs-Grt-liq triangular field limited by the Liq-in solidus curve and by the Ms-out/Als-in curve to temperatures of 690 °C $< T <$ 820 °C (green in Fig. 10). However, observing the composition of phases predicted by the model, reported as isopleths of relevant chemical parameters (Supplementary Fig. S1), it is apparent that these are very different from those actually measured in the sample. The disagreement is particularly large for garnet components, and for the Ti content of biotite, and confirms that the compositions of phases have been extensively reset during retrograde metamorphism. Since the mineral compositions do not help constrain anatectic *P-T* conditions, and because of the uncertainty to define exactly the phase assemblage during melting, an alternative thermobarometric approach can be adopted taking advantage of the thermometric information provided by remelting experiments. As the most realistic temperatures at which

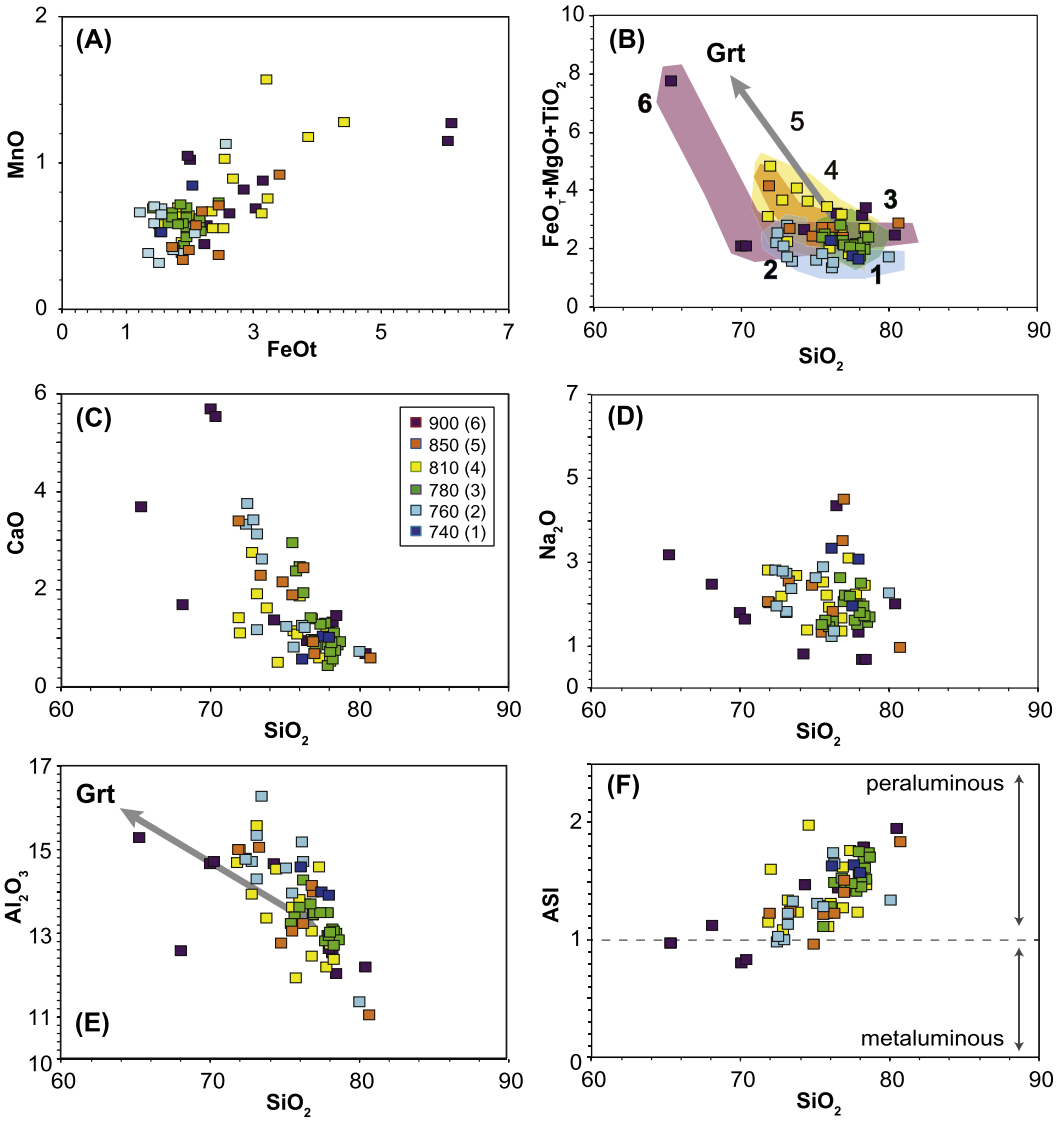

Fig. 6. Harker diagrams showing the major element concentrations (wt%) of melt inclusions in crustal enclaves after remelting experiments at 740 °C to 900 °C (data in Table 2). (A) MnO vs. FeO_t. (B) FeO_t + MgO + TiO_2 vs. SiO_2. (C) CaO vs. SiO_2. (D) Na_2O vs. SiO_2. (E) Al_2O_3 vs. SiO_2. (F) ASI (alumina saturation index) vs. SiO_2. The grey compositional vectors in (B) and (E) point from average glass composition at 780 °C to average core composition of host garnets.

garnet grew and trapped melt and fluid inclusions are in the range 760–780 °C, or slightly lower due to possible sluggish kinetics of experiments (Bartoli et al., 2013a), and considering that the melt and fluid entrapment occurred when the rocks had just entered the sillimanite stability field, peak *P-T* conditions corresponding to the orange field in Fig. 10 can be derived. The area is located between 740 and 780 °C and 0.7 to 0.9 GPa. Such apparently tight constraint is affected by the analytical and kinetic uncertainties implicit in respectively the modelling and the experimental remelting, which are in the order of some tens of °C and 0.1 GPa. If the inferred peak P-T conditions, and the corresponding equilibrium phase assemblage, are correct, then it follows that the abundant muscovite observed in the sample formed during the pervasive reequilibration at retrograde conditions.

5.2. Composition, fluid regime and volatile content of the primary melt

Our work provides the first data on the composition of natural anatectic melt produced by Al_2SiO_5-free, greywacke-like source rocks. The bulk composition of the studied sample, reported in Fig. 10, is very similar to the starting material CEVP used by Vielzeuf and Montel (1994) in their experimental investigation of the partial melting of metagreywackes. The sample studied here is slightly more potassic and less sodic, and contains more FeO_{tot}. The silica and alumina contents are virtually identical. In terms of major elements, the remelted inclusions in this work show a peraluminous leucogranitic to granitic composition with ASI in the range 1.0–1.7 (in the experiments at 760 and 780 °C). The production of a peraluminous granitic melt from an Al_2SiO_5-free protolith is in agreement with the experimental glass compositions measured by Montel and Vielzeuf (1997), even though that work explored temperatures >800°, higher than those inferred for anatexis in our sample.

From the fluid content point of view, there are few lines of evidence suggesting that partial melting of the investigated rocks occurred in the presence of a fluid phase, including i) the coexistence of primary FI and MI within the same cluster, and ii) the major element composition of primary melt.

The abundant FI coexisting with MI in the same cluster indicate the presence of a C-O-H fluid dominated by H_2O and CO_2. Graphite was not observed within the FI but carbonates (calcite and siderite) are common within garnets. Recently Carvalho et al. (2019) discussed the recovery of

C-O-H bearing FI in metasedimentary rocks from the Ivrea Zone at amphibolite to granulite facies conditions and argued that "a (graphitic) rock undergoing melting will always show the presence of a free C-O-H fluid, in variable amounts and with variable a_{H2O} depending on pressure, temperature and the bulk composition of the system". According to Carvalho et al. (2019), the fluid regime during anatexis might be characterized by CO_2-dominated fluid in processes dominated by dehydration of OH-bearing phases. In the Edixon Complex, where the fluid was likely H_2O dominated, conditions of entrapment are compatible with the beginning of partial melting and potentially with both muscovite and biotite fluid-present melting conditions. The calculated isomodes (not reported) suggest that muscovite and biotite are consumed at the solidus to produce limited amounts of melt and peritectic garnet, always in the absence of aluminum silicate. Since the muscovite fluid-present melting (without biotite) would produce peritectic aluminum silicate instead of garnet (Weinberg and Hasalová, 2015), the rock assemblage is more consistent with a muscovite + biotite fluid-present melting reaction (Weinberg and Hasalová, 2015). Increasing a_{H2O} should reduce garnet stability (Conrad et al., 1988; Gardien et al., 2000), but the experiments of Alonso-Perez et al. (2008) on Si-rich melts indicated the opposite, i.e. that stability of peritectic garnet increases with increasing H_2O in melt. Schwindinger et al. (2019) demonstrated by means of phase equilibria modelling that at 1 GPa the first appearance of garnet in anatectic metapelites is

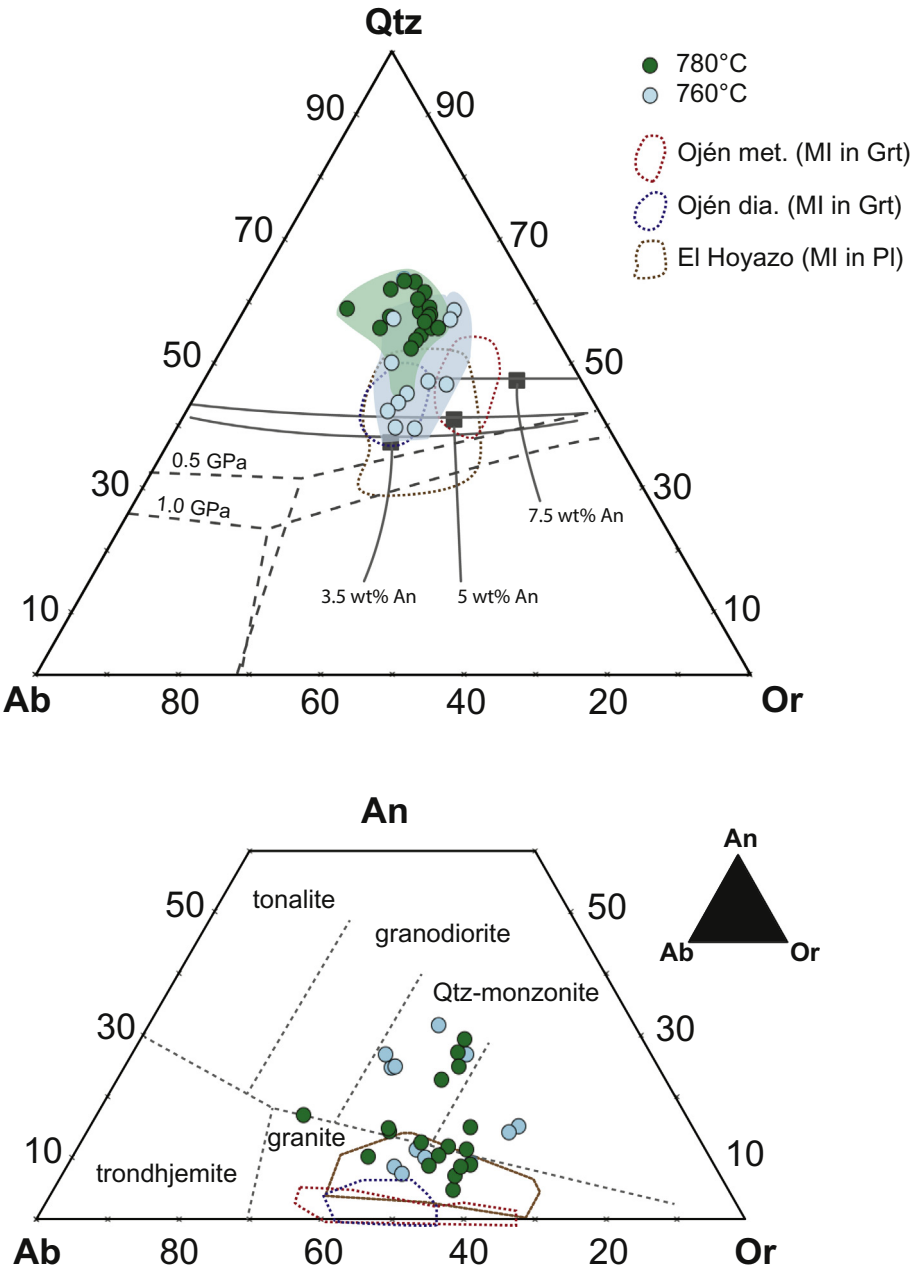

Fig. 7. CIPW Qz-Ab-Or and An-Ab-Or diagrams showing the normative compositions of all analyzed melt inclusions. Blue and green circles are for glassy inclusions remelted at 760 °C and 780 °C respectively. Grey dotted lines show the eutectic points and cotectic lines for the subaluminous haplogranite system at $aH_2O = 1$ and different pressures (Holtz and Johannes, 1992; Huang and Wyllie, 1975; Luth et al., 1964). Grey squares and lines represent the effect of different amounts of normative melt An at constant 0.1 GPa pressure (data from James and Hamilton, 1969). References to experimental glasses from experimentally remelted inclusions from Ojén (Bartoli et al., 2013c) and homogeneous glasses (not remelted) in inclusions from El Hoyazo (Acosta-Vigil et al., 2007) where "met." refers to metatexites, and "diat." to diatexite.

at 760 °C under dry conditions, whereas it occurs at 720 and 680 °C with 1 and 1.5 wt% H_2O added, respectively.

The H_2O content of glasses at 760 °C is more scattered (≈2–8 wt%) than at 780 °C (≈4–7 wt%) but in both cases the maxima are close to the values predicted for H_2O saturation at 0.8 GPa for haplogranitic melts (≈7.6 wt%; Holtz et al., 2001). The lower H_2O contents of some glasses may be explained as effect of heterogeneous distribution of the fluid (see discussion in Bartoli et al., 2014) and/or by the presence of a diluting carbonic species in the COH fluid, namely CO_2. The H_2O content of glasses determined as difference to 100 from EMPA analyses may yield similar contents, though Acosta-Vigil et al. (2016) report deviations up to 30%. In Table 2, the average difference to 100 total decreases with increasing experimental temperatures from ≈14 wt% at 740 °C to ≈12–11 wt% at 760–780 °C and ≈10–11 wt% at 810–900 °C. All values overestimate the measured H_2O in glasses. Possible explanations may account for the presence of light and incompatible elements as B, which is abundant in first anatectic products or micropores and would be consistent with the presence of tourmaline in the rock. Concerning other volatiles, the Cl and F content of the glasses was below the detection limits. This inconsistency requires further investigation.

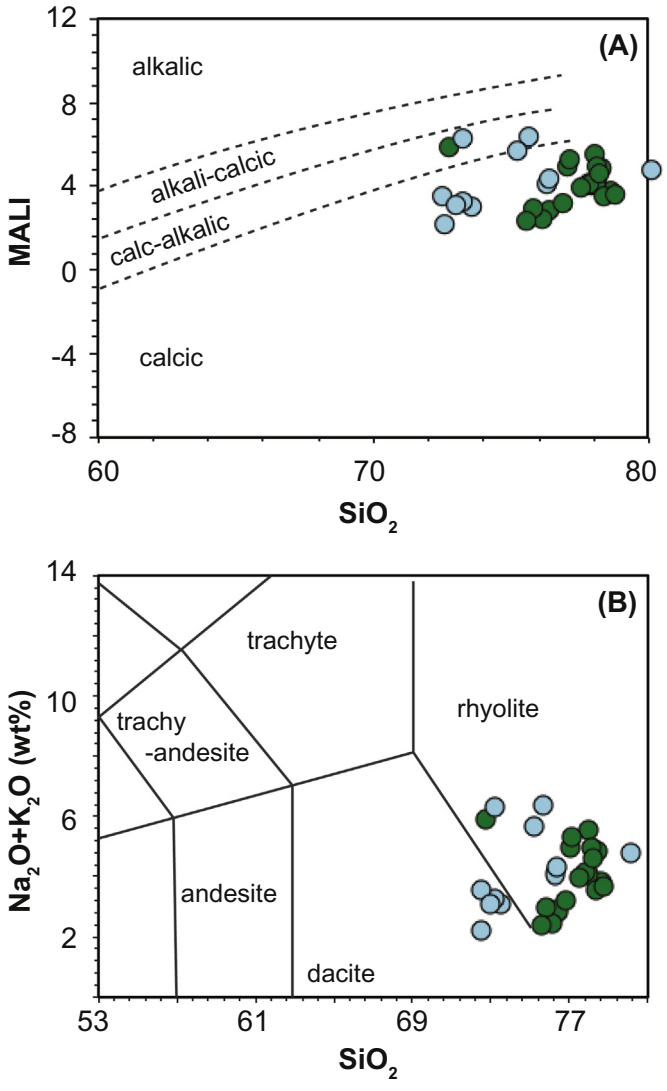

Fig. 8. Composition of analyzed melt inclusions in (A) modified alkali-lime index (MALI = $Na_2O + K_2O - CaO$) vs. SiO_2 (wt%) after Frost et al. (2001); (B) total alkali vs. SiO_2 diagram. Symbols as in Fig. 7.

The maximum CO_2 content of the remelted glasses from NanoSIMS (with all C calculated as CO_2) is 209–770 ppm at 760 °C and 541–2020 ppm at 780 °C (Fig. 9A). Such difference may be explained considering that i) the CO_2 solubility in felsic melts slightly increases with increasing T at least at 0.5 GPa (Tamic et al., 2001), ii) the CO_2 solubility and speciation are affected by the glass composition, with total CO_2 increasing with increasing SiO_2 and decreasing with increasing Na_2O, and molecular CO_2 prevailing on the $(CO_3)^{2-}$ species in SiO_2 rich- and Na_2O poor- compositions (Brooker et al., 1999). At 780 °C, glasses have higher SiO_2 and lower Na_2O with respect to glasses produced at 760 °C, so the CO_2 speciation is expected to be dominated by molecular CO_2. Even though most of the analyzed MI appeared homogeneous and bubble-free on polished surface, the presence of bubbles deep within the inclusion cannot be excluded. Since the fluid phase preserved in the bubble is mostly CO_2-rich (Fig. 4B) in agreement with Wallace et al. (2015), this may account for an additional CO_2 reservoir. If (slightly) higher resorption of the fluid bubbles takes place at increasing temperature, this may explain the higher CO_2 content of glasses remelted at 780 °C vs. 760 °C.

Granitic melt produced by water-present melting of metasedimentary rocks are expected to have higher ASI values than those produced by muscovite or biotite dehydration melting (Acosta-Vigil et al., 2003), to be enriched in Na_2O and CaO (Weinberg and Hasalová, 2015), and to contain higher proportion of MgO and FeO at increasing water content or water activity (e.g. Conrad et al., 1988; Holtz and Johannes, 1991) at constant P–T (Patiño Douce and Beard, 1996). This is partly consistent with the glass composition at 780 °C, with average ASI value of 1.50, MALI (= $Na_2O + K_2O$ - CaO) value of ≈4.1 ± 1.0 wt%, CaO content of ≈ 1.24 ± 0.7 wt% and $FeO_{tot} + MgO > 2.1$ wt %, supporting the hypothesis of fluid-saturated partial melting.

5.3. Anatexis and evolution of the Edixon Metamorphic Complex

The tectonometamorphic history of the Edixon Metamorphic Complex and its role in the evolution of the Wilson Terrane has been primarily constrained by investigations along the western Lanterman Range but also southward within a wider belt including Salamander Range and Niagara Icefalls-Mountaineer Range regions which are exposed, as the Lanterman Range, along the Lanterman fault (e.g., Ghiribelli, 2000; Ricci and Tessensohn, 2003; Talarico et al., 1998, 2004). Previous studies showed the presence of rocks with contrasting P-T paths in different localities of the EMC (Castelli et al., 2003; Ghiribelli, 2000; Talarico et al., 1998, 2004): a low P-high T metamorphism up to anatexis (Grt-Crd migmatites) characterized by a counterclockwise path with isobaric cooling has been recognized at the western Lanterman Range and at the Salamander Range (Ghiribelli, 2000). Peak conditions for migmatites were T ≈ 700 °C and P ≈ 0.5 GPa. Similar P-T conditions and path have been described in rocks outcropping at the internal Wilson Terrane (Palmeri, 1997; Palmeri et al., 1991, 1994).

In other localities of the EMC, as at the Mountaineer Range, a different P-T path involving an early decompression following a moderate thickening and a final cooling-unloading path has been inferred (Castelli et al., 2003). The T-P conditions for migmatites of the latter area are at ≈ 700–750 °C and ≈ 0.5–0.6 GPa (Castelli et al., 2003).

In this paper, the MI preserved in peritectic garnet and phase equilibria modelling demonstrate that the portion of the EMC close to Mt. Edixon experienced anatexis up to 760–780 °C at 0.7–0.9 GPa, corresponding to the P-T conditions of entrapment.

Even though it is not possible to reconstruct a proper P-T-relative time path based on sample GO5, the equilibrium conditions reconstructed from the remelting experiments and thermodynamic modelling allow extending the evolution of the EMC up to ca. ≈0.8 GPa at 760–780 °C. The latter data sustain that the EMC is not a homogeneous metamorphic complex (Ricci and Tessensohn, 2003). Instead, it represents a mélange of different crustal slices characterized by different P-T conditions for the high grade rocks, which support the interpretation

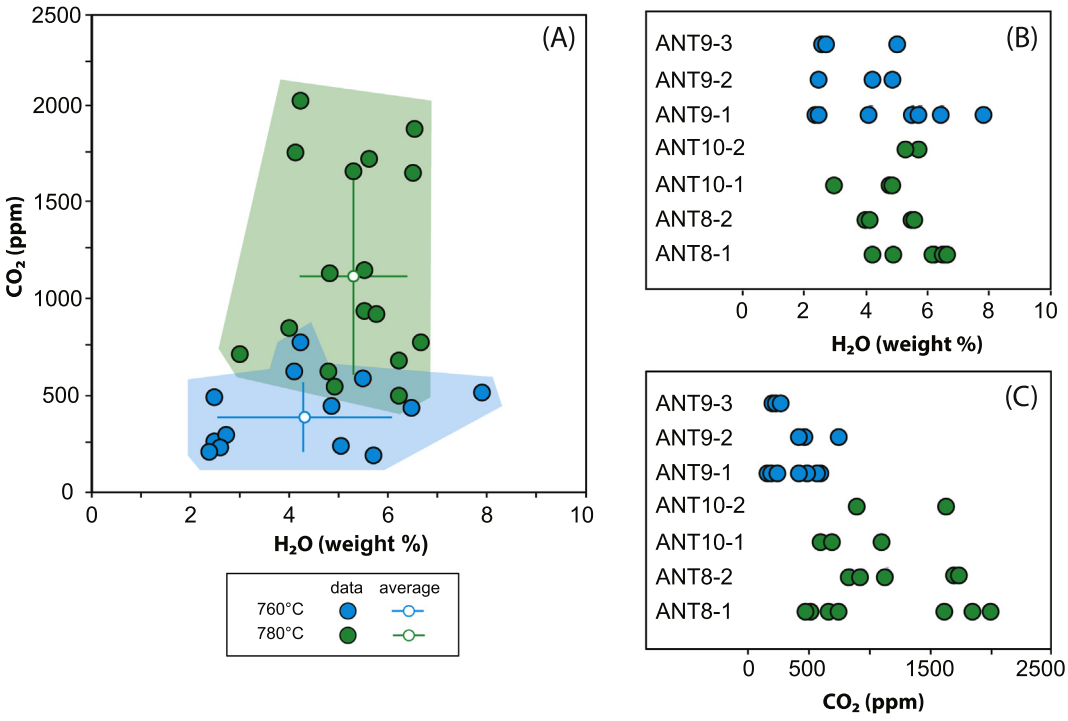

Fig. 9. H_2O and CO_2 concentration of re-homogenized melt inclusions in experiments performed at 760 °C (blue circles) and 780 °C (green circles) measured by NanoSIMS. White circles in (A) are averages of analyses at 760 °C and 780 °C. Horizontal and vertical bars are one standard deviation on average values.

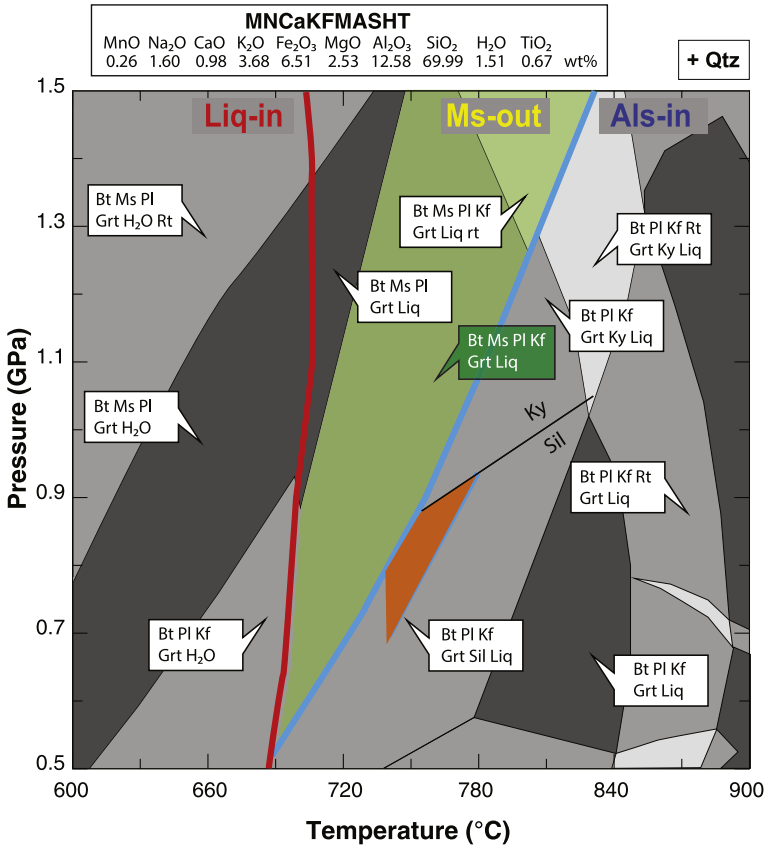

Fig. 10. (A) P–T section for GO5 calculated in MnNCaKFMASHT system (bulk composition from XRF analysis). The colored shaded fields indicate the peak P-T conditions compatible of the rock assemblage (green) and MI entrapment (orange, see text for details).

that anatexis in the EMC could have taken place at different crustal levels.

About the timing of anatexis in the study sample, some considerations could be made. Texturally and chemically similar white micas, in a micaschist of the EMC geographically close to GO5, yield an Ar^{39}-Ar^{40} age of nearly 480 Ma (Di Vincenzo et al., 2001). The latter Ar^{39}-Ar^{40} age is very diffuse along the Lanterman fault not only in white mica but also in biotite and amphibole (Di Vincenzo et al., 2001; Di Vincenzo and Palmeri, 2001). This age is interpreted as the Early Ordovician final "closure" of micas at the Lanterman Range (Di Vincenzo et al., 2001, 2016) and mainly referred to the exhumation process of the different complexes along the Lanterman fault. On the other hand, ages around 500–490 Ma, are also very common in the Wilson Terrane and along the Lanterman fault (Di Vincenzo et al., 2016 and reference therein; Goodge, 2020 and reference therein). The ages of 500–490 Ma are attributed to the main tectonometamorphic event due to the docking of the different tectonic slices along the Lanterman fault, triggered by the final collision and amalgamation of Bowers Terrane with the Wilson Terrane. The latter event is coeval with the late-tectonic fluid driven magmatism in the Wilson Terrane (Goodge, 2020 and reference therein) suggesting that MI formation of the EMC complex of the Lanterman Range, could be referred to the same tectonometamorphic event.

Supplementary data to this article can be found online at https://doi.org/10.1016/j.lithos.2020.105685.

Acknowledgements

This work was funded by the CaRiPaRo project Makearth (Cassa di Risparmio di Padova e Rovigo) to FF, by grant MIUR-PRIN 2017ZE49E7_003 to BC, the grants SIR RBSI14Y7PF (Italian Ministry of Education, University, Research) and BART_SID19_01 (University of Padova) to OB, the PNRA (PdR 13/B2.07) to RP and by the German Federal Ministry for Education and Research and the Deutsche Forschungsgemeinschaft (Project FE 1527/2-1 and FE 1527/2-2) to SF. The NanoSIMS facility at the Muséum National d'Histoire Naturelle in Paris was established by funds from the CNRS, Région Ile de France, Ministère délégué à l'Enseignement supérieur et à la Recherche, and the Muséum National d'Histoire Naturelle. The sample used in this study was collected by Gianni Capponi e Giacomo Oggiano and is available at the PNRA (Programma Nazionale Ricerche in Antartide) rock repository located at the Museo Nazionale dell'Antartide (Siena, Italy).

Declaration of Competing Interest

The authors declare that they have no known competing financial interests or personal relationships that could have appeared to influence the work reported in this paper.

References

Acosta-Vigil, A., London, D., Morgan, G.B., VI, Dewers, A, T., 2003. Solubility of excess alumina in hydrous granitic melts in equilibrium with peraluminous minerals at 700–800°C and 200MPa, and applications of the aluminum saturation index. Contrib. Mineral. Petrol. 146, 100–119.

Acosta-Vigil, A., London, D., Morgan VI, G.B., 2006. Experiments on the kinetics of partial melting of a leucogranite at 200 MPa H2O and 690–800°C: Compositional variability of melts during the onset of H2O-saturated crustal anatexis. Contrib. Mineral. Petrol. 151, 539–557.

Acosta-Vigil, A., Cesare, B., London, D., Morgan .V.I., G.B., 2007. Microstructures and composition of melt inclusions in a crustal anatectic environment, represented by metapelitic enclaves within El Hoyazo dacites, SE Spain. Chem. Geol. 235, 450–465.

Acosta-Vigil, A., Buick, I., Hermann, J., Cesare, B., Rubatto, D., London, D., Morgan .V.I., G.B., 2010. Mechanisms of crustal anatexis: a geochemical study of partially melted metapelitic enclaves and host dacite, SE Spain. J. Petrol. 51, 785–821.

Acosta-Vigil, A., Barich, A., Bartoli, O., et al., 2016. The composition of nanogranitoids in migmatites overlying the Ronda peridotites (Betic Cordillera, S Spain): the anatectic history of a polymetamorphic basement. Contrib. Mineral. Petrol. 171, 24. https://doi.org/10.1007/s00410-016-1230-3.

Acosta-Vigil, A., London, D., Morgan .V.I., G.B., Cesare, Buick, I., Hermann, J., Bartoli, O., 2017. Primary crustal melt compositions: Insights into the controls, mechanisms and timing of generation from kinetics experiments and melt inclusions. Lithos 286–287, 454–479. https://doi.org/10.1016/j.lithos.2017.05.020.

Alonso-Perez, R., Müntener, O., Ulmer, P., 2008. Igneous garnet and amphibole fractionation in the roots of island arcs: experimental constraints on andesitic liquids. Contrib. Mineral. Petrol. 157, 541–558. https://doi.org/10.1007/s00410-008-0351-8.

Aubaud, C., Withers, A.C., Hirschmann, M.M., Guan, Y., Leshin, L.A., Mackwell, S.J., Bell, D.R., 2007. Intercalibration of FTIR and SIMS for hydrogen measurements in glasses and nominally anhydrous minerals. Am. Mineral. 92, 811–828.

Bartoli, O., 2017. Phase equilibria modelling of residual migmatites and granulites: an evaluation of the melt-reintegration approach. J. Metamorph. Geol. 35, 919–942.

Bartoli, O., Cesare, B., 2020. Nanorocks: a 10-year-old story. Rendiconti Lincei. Sci. Fisich. Nat. 31, 249–257.

Bartoli, O., Cesare, B., Poli, S., Acosta-Vigil, A., Esposito, R., Turina, A., Bodnar, R.J., Angel, R.J., Hunter, J., 2013a. Nanogranite inclusions in migmatitic garnet: behavior during piston cylinder re-melting experiments. Geofluids 13, 405–420.

Bartoli, O., Cesare, B., Poli, S., Bodnar, R.J., Acosta-Vigil, A., Frezzotti, M.L., Meli, S., 2013b. Recovering the composition of melt and the fluid regime at the onset of crustal anatexis and S-type granite formation. Geology 41, 115–118.

Bartoli, O., Tajčmanová, L., Cesare, B., Acosta-Vigil, A., 2013c. Phase equilibria constraints on melting of stromatic migmatites from Ronda (S. Spain): insights on the formation of peritectic garnet. J. Metamorph. Geol. 31, 775–789.

Bartoli, O., Cesare, B., Remusat, L., Acosta-Vigil, A., Poli, S., 2014. The H_2O content of granite embryos. Earth Planet. Sci. Lett. 395, 281–290. https://doi.org/10.1016/j.epsl.2014.03.031.

Bartoli, O., Acosta-Vigil, A., Ferrero, S., Cesare, B., 2016a. Granitoid magmas preserved as melt inclusions in high-grade metamorphic rock. Am. Mineral. 101, 1543–1559.

Bartoli, O., Acosta-Vigil, A., Tajčmanová, L., Cesare, B., Bodnar, R.J., 2016b. Using nanogranitoids and phase equilibria modeling to unravel anatexis in the crustal footwall of the Ronda peridotites (Betic Cordillera, S Spain). Lithos 256, 282–299.

Bartoli, O., Acosta-Vigil, A., Cesare, B., Remusat, L., Gonzalez-Cano, A., Wälle, M., Tajčmanová, L., Langone, A., 2019. Geochemistry of Eocene-early Oligocene low-temperature crustal melts from Greater Himalayan Sequence (Nepal): a nanogranitoid perspective. Contrib. Mineral. Petrol. 174 (10), 82.

Behrens, H., Jantos, N., 2001. The effect of anhydrous composition on water solubility in granitic melts. Am. Mineral. 86, 14–20.

Boger, S.D., 2011. Antarctica – before and after Gondwana. Gondwana Res. 19, 335–371.

Bomparola, R.M., Belousova, E., Ghezzo, C., Griffin, W.L., O'Reilly, Y.O., 2006. Resetting of the U–Pb zircon system in Cambro-Ordovician intrusives of the deep freeze Range, northern Victoria Land, Antarctica. J. Petrol. 48, 327–364.

Borg, S.G., De Paolo, D.J., Smith, B.M., 1990. Isotopic structure and tectonics of the central Transantarctic Mountains. J. Geophys. Res. 95, 6647–6667.

Bradshaw, J.D., Laird, M.G., 1983. The pre-beacon geology of Northern Victoria Land. In: Oliver, R.L., James, P.R., Jago, J.B. (Eds.), Antarctic Earth Science. Australian Academy of Science, Canberra, pp. 98–101.

Brooker, R.A., Kohn, S.C., Holloway, J.R., McMillan, P.F., Carroll, M.R., 1999. Solubility, speciation and dissolution mechanisms for CO_2 in melts on the $NaAlO_2$–SiO_2 join. Geochim. Cosmochim. Acta 63 (21), 3549–3565.

Bureau, H., Trocellier, P., Shaw, C., Khodja, H., Bolfan-Casanova, N., Demouchy, S., 2003. Determination of the concentration of water dissolved in glasses and minerals using nuclear microprobe. Nucl. Instrum. Methods Phys. Res., Sect. B 210, 449–454.

Capponi, G., Crispini, L., Meccheri, M., 1999. Structural history and tectonic evolution of the boundary between the Wilson and Bowers Terranes, Lanterman Range, Northern Victoria Land, Antarctica. Tectonophysics 312, 249–266. https://doi.org/10.1016/S0040-1951(99)00174-2.

Capponi, G., Castorina, F., Di Pisa, A., Meccheri, M., Petrini, R., Villa, I.M., 2002. The meta-igneous rocks of the Barber Glacierarea (northern Victoria Land, Antarctica): a clue to theenigmatic Borchgrevink Orogeny? In: Gamble, J., Skinner, D.N.B., Henrys, S. (Eds.), Antarctica at the Close of Amillennium. 35. Royal Society of New Zealand Bulletin, pp. 99–104

Carvalho, B.B., Bartoli, O., Ferri, F., Cesare, B., Ferrero, S., Remusat, L., Capizzi, L.S., Poli, S., 2019. Anatexis and fluid regime of the deep continental crust: New clues from melt and fluid inclusions in metapelitic migmatites from ivrea zone (NW Italy). J. Metamorph. Geol. 37, 951–975.

Carvalho, B.B., Bartoli, O., Cesare, B., Tacchetto, T., Gianola, O., Ferri, F., Aradi, L.E., Szabó, C., 2020. Primary CO_2-bearing fluid inclusions in granulitic garnet usually do not survive. Earth Planet. Sci. Lett. 536, 116170.

Castelli, D., Oggiano, G., Talarico, F., Belluso, E., Colombo, F., 2003. Mineral chemistry and petrology of the Wilson Terrane Metamorphics from Retreat Hills to Lady Newnes Bay, northern Victoria Land, Antarctica. In: Ricci, C.A., Tessensohn, F. (Eds.), Aspects of a Suture Zone, Marner Glacier area Antarctica. 85. Geologisches Jahrbuch B, pp. 133–172.

Cawood, P., 2005. Terra Australis Orogen: Rodinia breakup and development of the Pacific and Iapetus margins of Gondwana during the Neoproterozoic and Paleozoic. Earth Sci. Rev. 69, 249–279.

Cesare, B., 1999. Multi-stage pseudomorphic replacement of garnet during polymetamorphism: 1. Microstructures and their interpretation. J. Metamorph. Geol. 17, 723–734. https://doi.org/10.1046/j.1525-1314.1999.00229.x.

Cesare, B., Acosta-Vigil, A., Bartoli, O., Ferrero, S., 2015. What can we learn from melt inclusions in migmatites and granulites? Lithos 239, 186–216.

Coggon, R., Holland, T.J.B., 2002. Mixing properties of phengiticmicas and revised garnet–phengite thermobarometers. J. Metamorph. Geol. 20, 683–696.

Connolly, J.A.D., 2009. The geodynamic equation of state: what and how. Geochem. Geophys. Geosyst. 10, Q10014.

Conrad, W.K., Nicholls, I.A., Wall, V.J., 1988. Water-saturated and -undersaturated melting of metaluminous and peraluminous crustal compositions at 10 kb: evidence for the origin of silicic magmas in the Taupo volcanic zone, New Zealand, and other occurrences. J. Petrol. 29, 765–803. https://doi.org/10.1093/petrology/29.4.765.

Crispini, L., Di Vincenzo, G., Palmeri, R., 2007. Petrology and 40Ar–39Ar dating of shear zones in the Lanterman Range (northern Victoria Land, Antarctica): implications for the metamorphic and temporal evolution at terrane boundaries. Mineral. Petrol. 89, 217–249. https://doi.org/10.1007/s00710-006-0164-2.

Di Vincenzo, G., Palmeri, R., 2001. An 40Ar-39Ar investigation of high-pressure metamorphism and the retrogressive history of mafic eclogites from the Lanterman Range (Antarctica): evidence against a simple temperature control on argon transport in amphibole. Contrib. Mineral. Petrol. 141, 15–35.

Di Vincenzo, G., Palmeri, R., Talarico, F., Andriessen, P.A.M., Ricci, C.A., 1997. Petrology and geochronology of eclogites from the Lanterman Range. Antarctica. J. Petrol. 38, 1391–1417.

Di Vincenzo, G., Ghiribelli, B., Giorgetti, G., Palmeri, R., 2001. Evidence of a close link between petrology and isotope records: constraints from SEM, EMP, TEM and in situ 40Ar–39Ar laser analyses on multiple generations of white micas (Lanterman Range, Antarctica). Earth Planet. Sci. Lett. 192, 389–405.

Di Vincenzo, G., Grande, A., Rossetti, F., 2014. Paleozoic siliciclastic rocks from northern Victoria Land (Antarctica): provenance, timing of deformation and implications for the Antarctica/Australia connection. Geol. Soc. Am. Bull. 126, 1416–1438.

Di Vincenzo, G., Horton, F., Palmeri, R., 2016. Protracted (~30 Ma) eclogite-facies metamorphism in northern Victoria Land (Antarctica): Implications for the geodynamics of the Ross/Delamerian Orogen. Gondwana Res. 40, 91–106.

Federico, L., Crispini, L., Capponi, G., 2010. Fault-slip analysis and transpressional tectonics: a study of Paleozoic structures in northern Victoria Land, Antarctica. J. Struct. Geol. 32, 667–684.

Ferrero, S., Bartoli, O., Cesare, B., Salvioli, Mariani, Acosta-Vigil, A., Cavallo, A., Groppo, C., Battiston, S., 2012. Microstructures of melt inclusions in anatectic metasedimentary rocks. J. Metamorph. Geol. 30, 303–322.

Ferrero, S., Wunder, B., Walczak, K., O'Brien, P.J., Ziemann, M.A., 2015. Preserved near ultrahigh-pressure melt from continental crust subducted to mantle depths. Geology 43, 447–450. https://doi.org/10.1130/G36534.1.

Ferrero, S., Godard, G., Palmeri, R., Wunder, B., Cesare, B., 2018. Partial melting of ultramafic granulites from Dronning Maud Land, Antarctica: Constraints from melt inclusions and thermodynamic modelling. Am. Mineral. 103, 610–622. https://doi.org/10.2138/am-2018-6214.

Frost, B.R., Barnes, C.G., Collins, W.J., Arculus, R.J., Ellis, D.J., Frost, C.D., 2001. A geochemical classification for granitic rocks. J. Petrol. 42, 2033–2048.

Gardien, V., Thompson, A.B., Ulmer, P., 2000. Melting of biotite + plagioclase + quartz gneisses: the role of H_2O in the stability of amphibole. J. Petrol. 41, 651–666. https://doi.org/10.1093/petrology/41.5.651.

Ghezzo, C., Baldelli, C., Biagini, R., Carmignani, L., Di Vincenzo, G., Gosso, G., Lelli, A., Lombardo, B., Montrasio, A., Pertusati, P.C., Salvini, F., 1989. Granitoids from the David Glacier ± Aviator Glacier segment of the Transantarctic Mountains (Victoria Land Antarctica). In: Ricci, C.A. (Ed.), Proceedings of the Meeting: Geosciences in Victoria Land, Antarctica, Siena, September 2–3 1987. Mem Soc Geol Ital, pp. 143–159.

Ghiribelli, B., 2000. Evoluzione tettonica e metamorfica del margine attivo del Gondwana: Lanterman e Salamander Ranges (Antartide) Unpublished Ph.D. Thesis Siena University, p. 127.

Ghiribelli, B., Frezzotti, M.L., Palmeri, R., 2002. Coesite in eclogites of the Lanterman Range (Antarctica): evidence from textural and raman spectroscopy studies. Eur. J. Mineral. 14, 355–360.

Goodge, J.W., 2020. Geological and tectonic evolution of the Transantarctic Mountains, from ancient craton to recent enigma. Gondwana Res. 80, 50–122. https://doi.org/10.1016/j.gr.2019.11.001.

Grew, E.S., Kleinschmidt, G., Schubert, W., 1984. Contrasting metamorphic belts in North Victoria Land, Antarctica. Geol. Jahrb. 253–263 B60.

Hiroi, Y., Hokada, T., Kato, M., et al., 2019. Felsite–nanogranite inclusions and three Al2SiO5 polymorphs in the same garnet in ultrahigh–temperature granulites from Rundvågshetta, Lützow–Holm complex, East Antarctica. J. Mineral. Petrol. Sci. 114, 60–78. https://doi.org/10.2465/jmps.181118.

Holland, T.J.B., Powell, R., 1998. An internally consistent ther- modynamic data set for phases of petrological interest. J. Metamorph. Geol. 16, 309–343.

Holland, T.J.B., Powell, R., 2003. Activity-composition relations for phases in petrological calculations: an asymmetric multicom- ponent formulation. Contrib. Mineral. Petrol. 145, 492–501.

Hollister, L.S., 1977. The reaction forming cordierite from garnet, the Khtada Lake Metamorphic complex, British Columbia. Can. Mineral. 15, 217–229.

Holness, M.B., Cesare, B., Sawyer, E.W., 2011. Melted rocks under the microscope: microstructures and their interpretation. Elements 7, 247–252.

Holtz, F., Johannes, W., 1991. Genesis of peraluminous granites I. experimental investigation of melt compositions at 3 and 5 kb and various H_2O activities. J. Petrol. 32, 935–958. https://doi.org/10.1093/petrology/32.5.935.

Holtz, F., Johannes, W., 1992. Peraluminous granites: the effect of alumina on melt composition and coexisting minerals. Trans. R. Soc. Edinb. Earth Sci. 83, 409–416. https://doi.org/10.1017/S0263593300008075.

Holtz, F., Johannes, W., Tamic, N., Behrens, H., 2001. Maximum and minimum water contents of granitic melts generated in the crust: A reevaluation and implications. Lithos 56, 1–14.

Huang, W.L., Wyllie, P.J., 1975. Melting reactions in the system $NaA1Si_3O_8$- $KA1Si_3O_8$-SiO_2 to 35 kilobars, dry and with excess water. J. Geol. 83, 737–748.

James, R.S., Hamilton, D.L., 1969. Phase relations in the system NaAlSi3O8–KAlSi3O8–CaAl2Si2O8–SiO2 at 1 kbar water vapour pressure. Contrib. Mineral. Petrol. 21, 111–141.

Kleinschmidt, G., Tessensohn, F., 1987. Early Paleozoic westward directed subduction at the Pacific continental margin of Antarctica, sixth Gondwana symposium. Am. Geophys. Union Geophys. Monograph 40, 89–105.

Luth, W.C., Jahns, R.H., Tuttle, O.F., 1964. The granite system at pressure of 4 to 10 kilobars. J. Geophys. Res. 69, 759–773.

Montel, J.-M., Vielzeuf, D., 1997. Partial melting of metagreywackes, Part II. Compositions of minerals and melts. Contrib. Mineral. Petrol. 128, 176–196.

Morgan, George B., London, David, 2005. The effect of current density on the electron microprobe analysis of alkali aluminosilicate glasses. Am. Mineral. 90, 1131–1138.

Newton, R.C., Charlu, T.V., Kleppa, O.J., 1980. Thermochemistry of high structural state plagioclases. Geochim. Cosmochim. Acta 44, 933–941.

Palmeri, R., 1997. P-T paths and migmatite formation: an example from deep freeze Range, northern Victoria Land, Antarctica. Lithos 42, 47–66.

Palmeri, R., Talarico, F., Meccheri, M., Oggiano, G., Pertusati, P.C., Rastelli, N., Ricci, C.A., 1991. Progressive Deformation and Low Pressure/High Temperature Metamorphism in the Deep Freeze Range, Wilson Terrane, Northern Victoria Land, Antarctica. vol. 46. Memorie della Società Geologica Italiana, pp. 179–195.

Palmeri, R., Pertusati, P.C., Ricci, C.A., Talarico, F., 1994. Late Proterozoic(?)–early Paleozoic of the active pacific margin of Gondwana: evidence from the southern Wilson terrane (northern Victoria Land, Antarctica). Terra Antartica 1, 5–9.

Palmeri, R., Ghiribelli, B., Talarico, F., Ricci, C.A., 2003. Ultra-high-pressure metamorphism in felsic rocks: the garnet-phengite gneisses and quartzites from the Lanterman Range. Antarctica. Eur. J. Mineral. 15, 513–525. https://doi.org/10.1127/0935-1221/2003/0015-0513.

Palmeri, R., Ghiribelli, B., Ranalli, G., Talarico, F., Ricci, C.A., 2007. Ultrahigh-pressure metamorphism and exhumation of garnet-bearing ultramafic rocks from the Lanterman Range (northern Victoria Land, Antarctica). J. Metamorph. Geol. 25, 225–243. https://doi.org/10.1111/j.1525-1314.2006.00686.x.

Palmeri, R., Frezzotti, M.L., Godard, G., Davies, J., 2009. Pressure-induced incipient amorphization of α-quartz and transition to coesite in an eclogite from Antarctica: a first record and some consequences. J. Metamorph. Geol. 27, 685–705.

Palmeri, R., Talarico, F.M., Ricci, C.A., 2011. Ultrahigh-pressure metamorphism at the Lanterman Range (northern Victoria Land, Antarctica). Geol. J. 46, 126–136.

Patiño Douce, A.E., Beard, J.S., 1996. Effects of P, f(O2) and Mg/Fe ratio on dehydration-melting of model metagraywackes. J. Petrol. 37, 999–1024.

Redler, C., Johnson, T.E., White, R.W., Kunz, B.E., 2012. Phase equilibrium constraints on a deep crustal metamorphic field gradient: Metapelitic rocks from the Ivrea Zone (NW Italy). J. Metamorph. Geol. 30, 235–254.

Ricci, C.A., Tessensohn, F., 2003. The Lanterman-Mariner suture: Antarctic evidence for active margin tectonics in Paleozoic Gondwana. Geol. Jahrb. 303–332 B85.

Roedder, E., 1984. Fluid inclusions. Min. Soc. Am. Reviews Mineral. 12, 644.

Schwindinger, M., Weinberg, R.F., Clos, F., 2019. Wet or dry? The difficulty of identifying the presence of water during crustal melting. J. Metamorph. Geol. 37, 339–358.

Stump, E., 1995. The Ross Orogen of the Transantarctic Mountains. Cambridge University Press, Cambridge, p. 284.

Tacchetto, T., Bartoli, O., Cesare, B., Berkesi, M., Aradi, L.E., Dumond, G., Szabó, C., 2019. Multiphase inclusions in peritectic garnet from granulites of the Athabasca granulite terrane (Canada): evidence of carbon recycling during Neoarchean crustal melting. Chem. Geol. 508, 197–209. https://doi.org/10.1016/j.chemgeo.2018.05.043.

Tajčmanová, L., Connolly, J.A.D., Cesare, B., 2009. A thermodynamic model for titanium and ferric iron solution in biotite. J. Metamorph. Geol. 27, 153–165.

Talarico, F., Borsi, L., Lombardo, B., 1995. Relict granulites in the Ross Orogen of northern Victoria Land (Antarctica), II. Geochemistry and palaeo-tectonic implications. Precambrian Res. 75, 157–174. https://doi.org/10.1016/0301-9268(95)80004-2.

Talarico, F., Ghiribelli, B., Smith, S.C., Palmeri, R., Ricci, C.A., 1998. The northern Victoria Land segment of the Antarctic paleo-Pacific margin of eastern Gondwana: new constraints from the Lanterman and Mountaineer Ranges. Terra Antartica 5, 245–252.

Talarico, F., Palmeri, R., Ricci, C.A., 2004. Regional metamorphism and P-T evolution of the Ross orogen in northern Victoria Land (Antarctica): A review. Periodico Mineralogia 73, 185–196.

Tamic, N., Behrens, H., Holtz, F., 2001. The solubility of H_2O and CO_2 in rhyolitic melts in equilibrium with a mixed CO_2-H_2O fluid phase. Chem. Geol. 174, 333–347.

Thomen, A., Robert, F., Remusat, L., 2014. Determination of the nitrogen abundance in organic materials by NanoSIMS quantitative imaging. J. Anal. At. Spectrom. 29, 512–519.

Thompson, J.B., Hovis, G.L., 1979. Entropy of mixing in sanidine. Am. Mineral. 64, 57–65.

Vielzeuf, D., Montel, J.-M., 1994. Partial melting of metagreywackes. Part 1. Fluid-absent experiments and phase relationships. Contrib. Mineral. Petrol. 117, 375–393.

Wallace, P.J., Kamenetsky, V.S., Cervantes, P., 2015. Melt inclusion CO_2 contents, pressures of olivine crystallization, and the problem of shrinkage bubbles. Am. Mineral. 100, 787–794 003-004X/15/0004–87$05.00/DOI:doi:10.2138/am-2015-5029.

Wang, X., Chou, I.M., Hu, W., Burruss, R.C., Sun, Q., Song, Y., 2011. Raman spectroscopic measurements of CO_2 density: Experimental calibration with high-pressure optical cell (HPOC) and fused silica capillary capsule (FSCC) with application to fluid inclusion observations. Geochim. Cosmochim. Acta 75, 4080–4093.

Weinberg, R.F., Hasalová, P., 2015. Water-fluxed melting of the continental crust: A review. Lithos 212, 158–188.

White, R.W., Powell, R., Holland, T.J.B., 2007. Progress relating to calculation of partial melting equilibria for metapelites. J. Metamorph. Geol. 25, 511–527.

Whitney, D.L., Evans, B.W., 2010. Abbreviations for names of rock-forming minerals. Am. Mineral. 95, 185–187.

Wilke, S., Holtz, F., Neave, D.A., Almeev, R., 2017. The effect of anorthite content and water on quartz–feldspar cotectic compositions in the rhyolitic system and implications for geobarometry. J. Petrol. 58 (4), 789–818. https://doi.org/10.1093/petrology/egx034 2017.